Mon. Not. R. Astron. Soc. **000**, 1–19 (2009) Printed 4 August 2009 (MN LATEX style file v2.2)

The interactions of winds from massive young stellar objects: X-ray emission, dynamics, and cavity evolution

E. R. Parkin[1⋆], J. M. Pittard[1]†, M. G. Hoare[1]‡, N. J. Wright[2]§, J. J. Drake[2]¶
[1] *School of Physics and Astronomy, The University of Leeds, Woodhouse Lane, Leeds LS2 9JT, UK*
[2] *Harvard-Smithsonian Center for Astrophysics, 60 Garden Street, Cambridge MA01238, USA*

Accepted ... Received ...; in original form ...

ABSTRACT

2D axis-symmetric hydrodynamical simulations are presented which explore the interaction of stellar and disk winds with surrounding infalling cloud material. The star, and its accompanying disk, blow winds inside a cavity cleared out by an earlier jet. The collision of the winds with their surroundings generates shock heated plasma which reaches temperatures up to $\sim 10^8$ K. Attenuated X-ray spectra are calculated from solving the equation of radiative transfer along lines-of-sight. This process is repeated at various epochs throughout the simulations to examine the evolution of the intrinsic and attenuated flux. We find that the dynamic nature of the wind-cavity interaction fuels intrinsic variability in the observed emission on timescales of several hundred years. This is principally due to variations in the position of the reverse shock which is influenced by changes in the shape of the cavity wall. The collision of the winds with the cavity wall can cause clumps of cloud material to be stripped away. Mixing of these clumps into the winds mass-loads the flow and enhances the X-ray emission measure. The position and shape of the reverse shock plays a key role in determining the strength and hardness of the X-ray emission. In some models the reverse shock is oblique to much of the stellar and disk outflows, whereas in others it is closely normal over a wide range of polar angles. For reasonable stellar and disk wind parameters the integrated count rate and spatial extent of the intensity peak for X-ray emission agree with *Chandra* observations of the deeply embedded MYSOs S106 IRS4, Mon R2 IRS3 A, and AFGL 2591.

The evolution of the cavity is heavily dependent on the ratio of the inflow and outflow ram pressures. The cavity closes up if the inflow is too strong, and rapidly widens if the outflowing winds are too strong. The velocity shear between the respective flows creates Kelvin-Helmholtz (KH) instabilities which corrugate the surface of the cavity. Rayleigh-Taylor-like instabilities also occur when the cavity wall is pushed forcefully backwards by strong outflows. The opening angle of the cavity plays a significant role and we find that for collimation factors in agreement with those observed for bi-polar jets around massive young stellar objects (MYSOs), a reverse shock is established within $\lesssim 500$ au of the star.

Key words: X-rays:stars - stars:winds, outflows - stars:formation - stars:early-type - hydrodynamics

1 INTRODUCTION

Observational and theoretical advances have provided increasing evidence that massive star formation is not merely a scaled up version of low mass star formation. The crucial difference arises from the prominent role of radiation pressure in massive star formation (Zinnecker & Yorke 2007, and references there-in). Theoretical models find that the radiation pressure from the core is too great for spherical accretion to form stars above a mass of $\sim 10\,\mathrm{M}_\odot$ (Wolfire & Cassinelli 1987). This problem disappears if one considers disk accretion (Yorke & Sonnhalter 2002; Krumholz et al. 2009). Observations of young massive stars support this scenario as they show the presence of a dense equatorial disk and

⋆ E-mail: erp@ast.leeds.ac.uk
† E-mail: jmp@ast.leeds.ac.uk
‡ E-mail: mgh@ast.leeds.ac.uk
§ E-mail: nwright@cfa.harvard.edu
¶ E-mail: jdrake@cfa.harvard.edu

ongoing accretion (Patel et al. 2005; Beltrán et al. 2006; Torrelles et al. 2007). There are, however, some similarities in the formation processes of both low and high mass stars. For instance, both involve outflows (Garay & Lizano 1999; Reipurth & Bally 2001; Banerjee & Pudritz 2006, 2007). Bi-polar cavities around YSOs are commonly observed in star formation (Garay & Lizano 1999), with collimation factors of $\sim 2-10$ for MYSOs (Beuther et al. 2002; Davis et al. 2004). The cavities may be more strongly collimated at large distances (due to their formation by jets), but less so at the base due to the action of stellar winds (Shepherd 2005). For low-mass stars the observed cavity morphology can be qualitatively reproduced by the injection of an outflow into a non-spherical density distribution (Delamarter et al. 2000; Lee et al. 2001; Wilkin & Stahler 2003; Mendoza et al. 2004; Cunningham et al. 2005). Magnetic fields increase the collimation (Gardiner et al. 2003; Shang et al. 2006). Numerical simulations of high-mass star formation show that outflows are a by-product of the collapse process which forms the massive star, and may be due to radiation pressure and magnetic fields (Yorke & Sonnhalter 2002; Banerjee & Pudritz 2007).

The widths of IR recombination line emission observed from MYSOs indicates the presence of dense outflows with velocities ranging from 100 to > 340 $\mathrm{km\,s^{-1}}$ (Drew et al. 1993; Bunn et al. 1995). Further confirmation of outflows has come from high angular resolution radio observations (e.g. Hoare et al. 1994; Hoare 2006). One explanation would be a disk wind generated when UV flux from the star is absorbed and re-emitted by the material at the surface of the disk.

Radiation-driven accretion disk winds have been previously explored using hydrodynamic models. Proga et al. (1998) and Drew et al. (1998) found that for a star-disk system where the $10\,\mathrm{M_\odot}$ star and it's accompanying disk were equally luminous (i.e. $L_*/L_{\rm disk}=1$), a strong steady disk wind could be produced. They found that there was a transition from a fast, low density polar outflow to a higher density outflow at a polar angle of $\theta \simeq 40-60^\circ$. The stellar wind had a velocity of $\simeq 2000$ $\mathrm{km\,s^{-1}}$, and the disk wind velocity ranged from $\simeq 400$ $\mathrm{km\,s^{-1}}$ at high latitudes to tens of $\mathrm{km\,s^{-1}}$ at low latitudes. They also found a density contrast of 10^2-10^4 between the stellar and disk winds, the latter being much denser. The opening angles of the stellar and disk winds are dependent on a number of parameters in the disk wind model: the luminosity ratio between the star and the disk, the force parameter used to calculate the radiative driving (Proga et al. 1999), and the magnetic pressure in the wind (Proga 2003). However, the assumption of strong magnetic fields in MYSO disks is speculative. The equatorial flow detected around S106 IRS4 (or IR) shows a mass-loss rate of $\dot{M} \simeq 10^{-6}\,\mathrm{M_\odot\,yr^{-1}}$ (Drew et al. 1993; Hoare et al. 1994), a factor of ~ 100 higher than the simulations. Such a difference could be accounted for by clumping in the wind. Sim et al. (2005) used a radiative transfer model inspired by disk wind simulations to model the HI line emission from MYSOs. They adopted a disk wind which was largely equatorial and had a velocity which declined from ~ 850 to $300\,\mathrm{km\,s^{-1}}$ in the angular range $82-89^\circ$. This model proved to be successful in reproducing qualitative features of Brackett and Pfund series line emission observations.

X-rays have been detected from deeply embedded MYSOs in star forming regions by the *Chandra X-ray observatory* (hereafter *Chandra*)(e.g. Broos et al. 2007; Wang et al. 2007, 2009). An initial observation of Mon R2 detected X-ray emission from the intermediate mass objects consistent with the hard and highly time variable X-ray emission caused by magnetic flaring activity between the star/disk (Kohno et al. 2002). Further analysis of the same data, coupled with high resolution near-IR interferometry identified the separate constituents of Mon R2 IRS3. Preibisch et al. (2002) found that the X-ray emission from IRS3 A and C, with a count rate of 0.166 ± 0.041 $\mathrm{ks^{-1}}$ for the former, could not be explained by the standard scenario for massive stars (i.e. wind embedded shocks produced by instabilities inherent in radiatively-driven winds - see Owocki et al. 1988), yet the estimated stellar masses of these objects implies they will have radiative outer envelopes which poses problems for the generation of X-rays through magnetic star/disk interactions. In their observations of the S106 region, Giardino et al. (2004) suggested that it may not be necessary to employ magnetic fields to explain the X-ray emission characteristics of the massive central object S106 IRS4 where the count rate was 0.30 ± 0.11 $\mathrm{ks^{-1}}$.

A potential source of X-rays which has not been considered before is the collision between the stellar and disk winds and the infalling envelope. To explore this interaction we perform the first detailed modelling of an MYSO embedded at the centre of a bi-polar cavity. The star and disk drive supersonic outflows, and we examine how these outflows influence the evolution of the infalling envelope. We find that the wind-cavity interaction produces a reverse shock where gas is heated to X-ray emitting temperatures. Our models are able to reproduce the observed count rates, although there is a strong sensitivity to the inclination angle of the observer.

This paper is organised as follows: § 2 gives a description of the model used in the simulations. The results of the simulations and the observable X-ray emission are presented in § 3. In § 4 we report on a recent observation of the MYSO AFGL 2591 with *Chandra* then perform fits to this observation and those of two other candidate objects, § 5 includes discussion, and in § 6 we summarize the conclusions from the current work and suggest possible future directions.

2 THE MODEL

Our model is of a recently formed massive star with an accompanying accretion disk. The star and disk are situated at the centre of a flattened envelope with a pre-existing bi-polar cavity evacuated by earlier jet activity. The morphology of the cavity is prescribed by a simple analytic equation. A schematic of the simulation domain is shown in Fig. 1.

The cavity intersects the disk plane at the cavity radius, $r_{\rm cav}$. In essence, the presence of a disk is implied through the presence of the disk wind, yet we do not include any parameters for the disk itself. We simply note that the disk wind is launched from the inner regions of the disk (i.e. $r \lesssim 10\,\mathrm{R_*}$, Drew et al. 1998). The star and disk are situated in the first cell within the simulation domain. Initially the cavity is filled with unshocked stellar and disk wind material, with the density and velocity a function of the polar angle, θ. The material outside of the cavity is infalling, and represents molecular gas which is still accreting onto the disk.

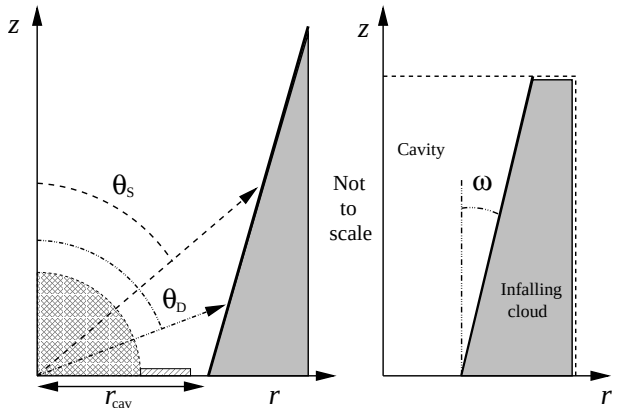

Figure 1. Schematic of the simulation domain. The left-hand panel shows a zoom in of the region close to the star and disk. The right panel shows the entire simulation domain, with dotted-line representing the edge of the grid. The cross-hatched quadrant in the left-hand panel represents the region where the winds are mapped onto the grid and the adjacent rectangular region represents the additional cells used to ensure the angular dependence of the wind is resolved (see § 2.2).

Features of the model, details of the hydrodynamics code used, and a description of the X-ray calculations are now given.

2.1 The infalling cloud

For the cloud material we use the solutions for the collapse of a slowly rotating isothermal sphere with a single point source of gravity at the centre (Ulrich 1976; Cassen & Moosman 1981; Chevalier 1983; Terebey et al. 1984). With conservation of angular momentum for infalling material the trajectories are parabolic and are described by the streamline equation (in polar coordinates),

$$\zeta = \frac{r_{\rm c}}{R} = \frac{\mu_0 - \mu}{(1-\mu_0^2)\mu_0} \tag{1}$$

where $\mu = \cos\theta$, $\mu_0 = \cos\theta_0$, and $R = \sqrt{z^2+r^2}$. $r_{\rm c}$ is the centrifugal radius of the cloud and θ_0 is the initial polar angle. The components of the infall velocity are given by,

$$\begin{aligned} u_{\rm R} &= -(\tfrac{GM_*}{R})^{1/2}(1+\tfrac{\mu}{\mu_0}), \\ u_\theta &= (\tfrac{GM_*}{R})^{1/2}(\tfrac{\mu_0-\mu}{\sin\theta})(1+\tfrac{\mu}{\mu_0})^{1/2}, \\ u_\phi &= (\tfrac{GM_*}{R})^{1/2}\tfrac{\sin\theta_0}{\sin\theta}(1-\tfrac{\mu}{\mu_0})^{1/2}. \end{aligned} \tag{2}$$

The density for the cloud material is then found by integrating the mass flux along streamlines,

$$\rho = \frac{-\dot{M}_{\rm infall}}{4\pi R^2 u_{\rm R}}[1+(3\mu_0^2-1)\zeta]^{-1}. \tag{3}$$

The infalling cloud material is assumed to be molecular gas at a temperature of 100 K.

2.2 The winds

Following the detection of equatorial winds from MYSOs (Drew et al. 1993; Hoare et al. 1994; Bunn et al. 1995; Hoare 2006) we choose to incorporate a disk wind into our model. The wind geometry we adopt is aimed at representing the characteristics of disk wind models. In particular we base our wind geometry on the hydrodynamical model of Drew et al. (1998) and the angle dependent model constructed by Sim et al. (2005). In these works the disk wind is assumed to be launched from the inner region ($< 10\ R_*$) of the accretion disk. A considerable difficulty in constructing this model is the range of scales across which important physics occurs. The cavity has dimensions of the order of 10^{16} cm, whereas the acceleration region of the winds is $\lesssim 10^{12}$ cm. Therefore, to represent the winds we have adopted a simple latitude dependent prescription, where the winds are mapped on with terminal velocities, which aims to capture the important features of a stellar/disk wind combination. The mass-loss rate is then,

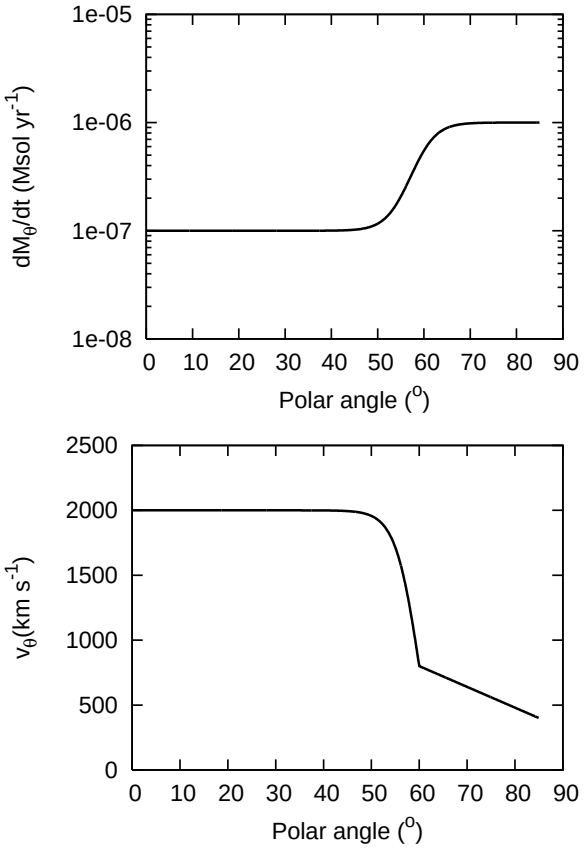

Figure 2. Variation of the angle dependent mass-loss rate, $\dot{M}_\theta$ (upper panel) and wind velocity, v_θ (lower panel) as a function of polar angle, θ, for model R1.

$$\begin{aligned} \dot{M}_\theta &= \frac{\dot{M}_{\rm D}}{2}\left[1+\lambda+(1-\lambda)\tanh((\theta-\theta_{\rm S})\chi)\right], \\ \lambda &= \dot{M}_{\rm S}/\dot{M}_{\rm D} \end{aligned} \tag{4}$$

$\dot{M}_\theta$ is the mass-loss rate of the outflow (stellar and disk winds) as a function of polar angle, $\theta_{\rm S}$ is the transition angle between the stellar and disk winds, and χ is a steepening factor to sharpen the transition from the stellar wind to the disk wind (consequently, the frictional heating between the two flows is linked to this parameter). $\dot{M}_{\rm S}$ and $\dot{M}_{\rm D}$ would be the mass-loss rates of the stellar and disk wind, respectively,

if the mass-loss was isotropic and spherical. Therefore, the *actual* net mass-loss rates of the stellar and disk winds can be found by integrating $\dot{M}_\theta$ over the appropriate angular range. We set $\chi = 5$. The wind velocity as a function of polar angle, v_θ, is,

$$v_\theta = \begin{cases} \frac{v_{\rm D}}{3}\left[1+\gamma+(1-2\gamma)\tanh((\theta-\theta_{\rm S})\chi)\right] & ;0<\theta\lesssim\theta_{\rm S} \\ \frac{v_{\rm D}}{3}\left[1+\gamma+(2-\gamma)(\frac{\theta-\theta_{\rm S}}{\theta_{\rm D}-\theta_{\rm S}})\right] & ;\theta_{\rm S}<\theta\lesssim\theta_{\rm D} \\ 0 & ;\theta_{\rm D}<\theta\lesssim\pi/2 \end{cases} \quad (5)$$

where $\gamma = v_{\rm S}/v_{\rm D}$, $v_{\rm S}$ and $v_{\rm D}$ are the terminal velocities of the stellar and disk winds respectively, and $\theta_{\rm D}$ is the transition angle above which there is no wind blown from the disk. The wind density as a function of polar angle is then calculated from,

$$\rho_\theta = \frac{\dot{M}_\theta}{4\pi R^2 v_\theta} \quad (6)$$

The angle dependent mass-loss rate and velocity profiles for model R1 are shown in Fig. 2. The winds are mapped into cells within a small radius of the grid origin ($\simeq 1\times10^{15}$ cm) provided that prior to the mapping a cell contains wind material (i.e. not inflowing cloud material). When necessary, additional cells in the first row above the disk plane (the r-axis in the model) are used to map on the winds (i.e. when $\theta_{\rm D} \simeq 89^\circ$). This is to ensure that the angular dependence of the disk wind is resolved sufficiently. The stellar and disk winds are switched on at $t = 0$. The unshocked winds are assumed to be ionized gas at a temperature of 10^4 K.

2.3 The cavity

In the model the initially un-shocked stellar/disk winds are separated from the infalling cloud material by a cavity wall. The shape and position of the cavity wall is described by a simple analytical prescription relating z and r on its surface (Alvarez et al. 2004a),

$$z = \left[\left(\frac{r}{r_{\rm cav}}\right)^\beta - 1\right]\kappa, \quad (7)$$

$$\text{where} \quad \kappa = \frac{a\cos\omega}{(\frac{a}{r_{\rm cav}}\sin\omega)^\beta - 1}. \quad (8)$$

ω is the half opening angle of the cavity, β controls the initial curvature of the cavity wall ($\beta = 1$ or 2 corresponds to a cavity wall with either a straight or parabolic shape), and a is a characteristic scale size of the cavity (we assume that $a = 8\times10^{16}$ cm, approximately in agreement with length scales for bi-polar outflows around MYSOs). It should be noted that Eq. 8 is only suitable for $\omega \gtrsim 3^\circ$.

2.4 The hydrodynamical code

To perform the simulations we use the hydrodynamical code VH-1 (Blondin et al. 1990). The code utilizes the Piecewise Parabolic Method (Colella & Woodward 1984) to solve the gas dynamics equations at cell boundaries. The version of the code we use in this work has undergone some modifications which include: radiative cooling (Strickland & Blondin 1995), a direct Eulerian solver, and portability to multi-processor machines using the message passing interface (MPI) via the grid parallelization scheme described in Saxton et al. (2005). We include radiative cooling for optically thin gas above $T = 10^4$ K, and assume that molecular gas below this temperature instantaneously cools to a temperature of $T = 10^2$ K. Gravity and rotation due to a central point source are incorporated through effective potential terms. The code also includes advected scalar fluid variables (dyes) which are used to trace the position of the separate components of the flow, i.e. stellar wind, disk wind, or cloud material.

We use a 2D, cylindrically symmetric, fixed grid with constant resolution throughout the simulations of $\delta z = \delta r = 8.\dot{3}\times10^{13}$ cm, which for the grid of the fiducial model (R1 in Table 1) equates to $r \times z = (5\times10^{16}\,{\rm cm})\times(8\times10^{16}\,{\rm cm}) = 600\times960$ cells. The boundary conditions (BCs) are set as follows: the $r = 0$ boundary uses a symmetric BC, the $z = 0$ boundary uses an outflow BC (to allow gas to flow onto a hypothetical disk). The $z = z_{\rm max}$ and $r = r_{\rm max}$ boundaries use either a zero-gradient outflow BC if the cell adjacent to the boundary is wind material or a fixed inflow condition for cloud material if the adjacent cell contains cloud material. In the latter case Eqs. 2 and 3 are used to populate the ghost cells.

2.5 X-ray emission

To allow a comparison to be made between *Chandra* X-ray observations of MYSOs and our simulations we calculate attenuated X-ray fluxes. Radiative transfer calculations are performed on the 2D models using the method described in Dougherty et al. (2003). This involves calculating emission and absorption coefficients for each cell on the grid and integrating the radiative transfer equation. For the emissivities we use values for optically thin gas in collisional ionization equilibrium obtained from look-up tables calculated from the MEKAL plasma code (Liedahl et al. 1995, and references there-in) containing 200 logarithmically spaced energy bins in the range 0.1-10 keV, and 101 logarithmically spaced bins in the range 10^4-10^9 K. Solar abundances are assumed. The advected fluid variables (dyes) are used to identify the X-ray emission contributions from the stellar and disk winds and the heated cloud material.

For lines-of-sight which exit the grid while in infalling cloud material we calculate an additional column density beyond the grid boundary by numerically integrating Eq. 3. X-rays which pass through the disk plane within the cavity radius, $r_{\rm cav}$, are assumed to be occulted by the accretion disk. For certain viewing angles there are lines-of-sight which exit the grid while in the stellar or disk winds. The winds have a much lower density than the cloud material, and therefore contribute far less absorption. The model cannot be used to calculate the attenuated emission for inclination angles smaller than the cavity opening angle due to insufficient extent of the computational grid (in reality there is likely to be additional absorption from swept-up cloud material formerly in the cavity).

Once model fluxes have been calculated we use the *Chandra* ACIS-I effective area[1] to convert the synthetic spectra into counts space. When calculating the synthetic fluxes we assume a distance to the MYSO of 1 kpc and an

[1] http://cxc.harvard.edu/cgi-bin/build_viewer.cgi?ea

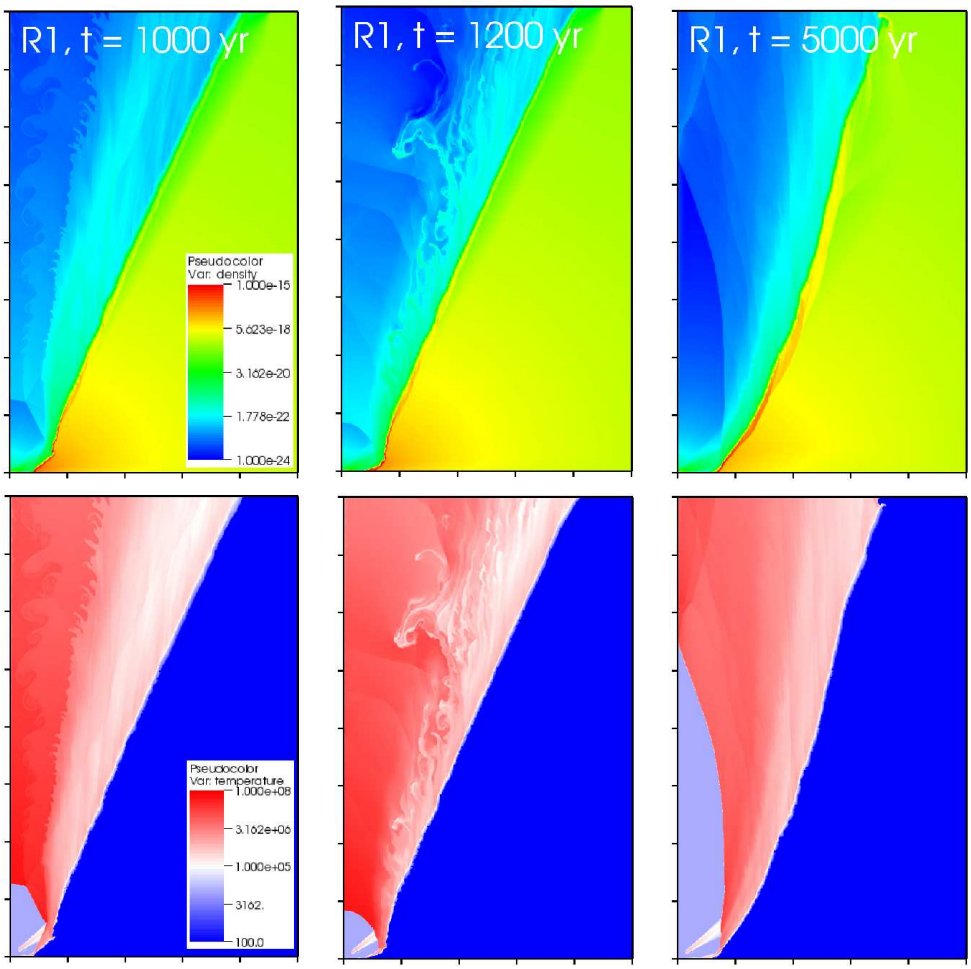

Figure 3. Snapshots of density (upper panels) and temperature (lower panels) taken from model R1 at (from left to right): $t = 1000$, 1200, and 5000 yr. The tick marks on the axis correspond to a distance of 10^{16} cm. The strip of $T \sim 10^5$ K gas which extends diagonally from the wind source is due to frictional heating at the interface between the fast stellar wind and the slower disk wind.

ISM column (between the observer at Earth and the edge of the cloud) of 1.9×10^{21} cm^{-2}.

3 RESULTS

To explore the impact of varying the different parameters in the model on both the evolution of the cavity and the resulting X-ray emission we have performed an extensive parameter space exploration (Table 1). Each simulation is allowed to run until a model time of 2000 yr, except model R1 which was allowed to run until a model time of 5000 yr. We first describe the cavity evolution and X-ray emission features of the fiducial model (R1), and then examine the influence of the various parameters on the results.

3.1 The standard model

3.1.1 Dynamical and X-ray properties

The standard model (R1) mimics the MYSO disk wind model of Drew et al. (1998), with identical wind geometry and stellar and disk wind velocities. The disk wind mass-loss rate is chosen to match observations (Felli et al. 1984). The stellar wind speed and mass-loss rate are representative of an O8-9V star[2] (Howarth & Prinja 1989). The mass infall rate for accretion onto the disk, $\dot{M}_{\rm infall}$, is chosen to be intermediate between the value of 1.1×10^{-4} M$_\odot$ yr^{-1} derived by Alvarez et al. (2004a) for the MYSO Mon R2 IRS 3A, and theoretically predicted mass infall rates of $\simeq 10^{-3}$ M$_\odot$ yr^{-1} for massive stars (Banerjee & Pudritz 2007; Krumholz et al. 2009). The centrifugal radius of the cloud, $r_{\rm c}$, is taken to be of the order of the observed disk radius for MYSOs (e.g. Alvarez et al. 2004a). As a simple first approximation the cavity radius, $r_{\rm cav}$, is taken to be equal to the centrifugal radius of the cloud, and the cavity is assumed to be conical ($\beta = 1$).

Fig. 3 shows the spatial distribution of material in the simulation; the disk wind lines the cavity wall and separates

[2] The stellar mass adopted in the simulations of 10 M$_\odot$ is lower than that expected for an 08-9V star ($\sim$ 30 M$_\odot$). An increase in the mass of the central star will increase the gravitational attraction felt by the infalling cloud material, and thus the infall velocity will increase and the density will be decreased. However, tests show that this difference does not significantly affect the results.

Table 1. List of the parameters used in the simulations. β is the parameter which defines the curvature of the cavity wall (Eq. 8), $r_{\rm c}$ is the centrifugal radius, ω is the cavity half opening angle, $\dot{M}_{\rm infall}$ is the mass infall rate of the molecular cloud, $\theta_{\rm S}$ is the transition angle between the stellar and disk wind, and $\theta_{\rm D}$ is the limiting angle above which there is no wind (i.e. only an accretion flow). For the wind terminal velocity, v, mass-loss rate, $\dot{M}$, and power, ζ, the subscripts "S" and "D" refer to the stellar and disk wind components, respectively. $M_* = 10$ M$_\odot$ and $r_{\rm cav} = 3.0 \times 10^{15}$ cm in all models, except models AFGL 2591 and Mon R2 where $r_{\rm cav} = 4.5 \times 10^{15}$ and 1.5×10^{15} cm, respectively.

Model	β	$r_{\rm c}$ (cm)	ω (°)	$\dot{M}_{\rm infall}$ (M$_\odot$ yr^{-1})	$\theta_{\rm S}$ (°)	$\theta_{\rm D}$ (°)	$v_{\rm S}$ (km s^{-1})	$v_{\rm D}$ (km s^{-1})	$\dot{M}_{\rm S}$ (M$_\odot$ yr^{-1})	$\dot{M}_{\rm D}$ (M$_\odot$ yr^{-1})	$\zeta_{\rm S}$ (L$_\odot$)	$\zeta_{\rm D}$ (L$_\odot$)
R1	1	3×10^{15}	30	2×10^{-4}	60	85	2000	400	1×10^{-7}	1×10^{-6}	250	132
R2	1	3×10^{15}	30	1×10^{-4}	60	85	2000	400	1×10^{-7}	1×10^{-6}	250	132
R3	1	3×10^{15}	30	1×10^{-3}	60	85	2000	400	1×10^{-7}	1×10^{-6}	250	132
R4	1	3×10^{15}	30	2×10^{-4}	60	85	2000	400	1×10^{-6}	1×10^{-6}	1674	158
R5	1	3×10^{15}	30	2×10^{-5}	60	85	2000	400	1×10^{-7}	1×10^{-7}	167	16
R6	1	3×10^{15}	30	1×10^{-3}	60	85	2000	400	1×10^{-7}	2×10^{-6}	343	261
R7	1	3×10^{15}	30	2×10^{-4}	60	85	2000	400	5×10^{-8}	1×10^{-6}	171	131
R8	1	3×10^{15}	30	2×10^{-4}	60	85	3000	400	1×10^{-7}	1×10^{-6}	555	218
R9	1	3×10^{15}	30	2×10^{-4}	60	85	1000	400	1×10^{-6}	1×10^{-6}	427	80
R10	1	3×10^{15}	30	2.5×10^{-5}	60	85	1000	400	2×10^{-8}	2×10^{-7}	12	15
R11	1	3×10^{15}	30	2×10^{-4}	70	85	2000	400	1×10^{-7}	1×10^{-6}	322	75
R12	1	3×10^{15}	30	2×10^{-4}	85	89	2000	400	1×10^{-7}	1×10^{-6}	433	21
R13	1	3×10^{15}	30	2×10^{-4}	–	–	2000	–	1×10^{-7}	–	470	–
R14	1	3×10^{15}	5	2×10^{-4}	60	85	2000	400	1×10^{-7}	1×10^{-6}	250	132
R15	1	3×10^{15}	10	2×10^{-4}	60	85	2000	400	1×10^{-7}	1×10^{-6}	250	132
R16	1	3×10^{15}	45	2×10^{-4}	60	85	2000	400	1×10^{-7}	1×10^{-6}	250	132
R17	1	3×10^{15}	60	2×10^{-4}	60	85	2000	400	1×10^{-7}	1×10^{-6}	250	132
R18	2	3×10^{15}	30	2×10^{-4}	60	85	2000	400	1×10^{-7}	1×10^{-6}	250	132
R19	1	8×10^{14}	30	2×10^{-4}	60	85	2000	400	1×10^{-7}	1×10^{-6}	250	132
R20	1	6×10^{15}	30	2×10^{-4}	60	85	2000	400	1×10^{-7}	1×10^{-6}	250	132
S106	1	3×10^{15}	50	3×10^{-5}	60	85	1000	350	4×10^{-8}	4×10^{-7}	24	25
Mon R2	1	8×10^{14}	10	2×10^{-5}	60	85	2000	400	1×10^{-8}	1×10^{-7}	23	14
AFGL 2591	1	4.5×10^{15}	15	3×10^{-4}	60	85	2000	400	1×10^{-7}	1×10^{-6}	250	132

the stellar wind from the infalling molecular cloud material. Close to the star there is a small strip of frictionally heated wind gas which reaches temperatures of $\sim 10^5$ K and therefore emits soft X-rays ($E \sim 0.1$ keV), although with a negligible observed flux when compared to the shocked winds. The stellar and disk winds in the simulations are supersonic, so that flow incident against the cavity wall results in shocked gas bounded by a reverse shock (this is best seen in the temperature images in Fig. 3). The postshock temperature is dictated by the preshock wind speed normal to the shock. For $v_{\rm S} = 2000$ km s^{-1}, temperatures up to $T \sim 10^8$ K are obtained, whereas the slower disk wind ($v_{\rm D} = 400$ km s^{-1}) is shocked only up to temperatures $\sim 10^{6.5}$ K. At the base of the cavity wall the small angle of incidence to the normal for the winds, and thus small angle of reflection, causes the shocked winds to intersect the rotational symmetry axis and close off the unshocked stellar wind. A pressure balance between the shocked and unshocked gas causes the reverse shock to continually enclose the latter. The reverse shock is almost normal to the preshock flow near the disk plane and on the symmetry axis where the highest postshock temperatures are obtained. Because the ram pressure of the inflow/outflow is angle dependent and the base of the cavity is subject to instabilities the shape of the reverse shock is often non-spherical. In Fig. 3 the reverse shock can be seen in the bottom left of the grid, where the enclosed preshock wind has temperature $T = 10^4$ K. The position of the reverse shock oscillates and its shape changes with time, due to small fluctuations in the shape and size of the base of the cavity wall as inflowing material is ablated and incorporated into the outflow, and as new inflowing material replenishes it. The size of the reverse shock is tied to the postshock pressure. The oscillations have a large effect on the observed emission as the postshock density, and therefore the emission measure, are dependent on the shock position. The postshock stellar wind has velocity vectors which are preferentially aligned in the polar direction. Small kinks to the shape of the reverse shock cause shear velocities in the post-shock flow, and KH instabilities are produced which can clearly be seen at $t = 1000$ yrs. The shear layer between the stellar and disk winds provides a site for the growth of $\sim 10^{16}$ cm amplitude KH instabilities on timescales of $\sim$ a few years. By $t = 1200$ yrs an instability of this proportion can be seen driving a clump of disk wind material into the path of the stellar wind, which leads

to mass-loading of the latter (for a review of mass-loading processes see Pittard 2007).

On larger scales the half opening angle of the cavity, ω, decreases until a temporary pressure balance is attained between the gas on either side of the cavity wall at $t \simeq 1000$ yr. A dense layer of compressed cloud material which grows with time results from the pile-up of inflowing cloud material. At the top of the cavity a small narrowing has occured due to the pressure difference across the cavity wall; if no winds are blown at all the cavity closes up over the star after ~ 500 yrs. Tests performed using the streamline equation (Eq. 1) to calculate the initial cavity shape and position did not prevent this occurence. By a simulation time of $t = 2000$ yr, the cavity has widened slightly at the base. The inflowing cloud material can still reach the disk plane and it is conceivable that accretion onto a disk could still be on-going while the winds are interacting with the cavity.

Model R1 was allowed to run for an extended simulation time of 5000 yr. At $t > 2000$ yr the shape of the cavity wall continues to change. The base of the cavity wall becomes more curved as time goes on, and the cavity wall at the top of the grid narrows further (Fig. 3). The spectrum at $t = 5000$ yrs has a very similar shape to that at 1000 yrs, though with a factor of ~ 2 lower normalization (Fig. 7). Similarly, the *Chandra* count rate is lower (model $\mathrm{R1_{long}}$ in Table 2). These differences are unsurprising as the reverse shock is now further from the star.

The X-ray emissivity of the shocked gas varies enormously with position. The intrinsic X-ray emission comes mainly from disturbed cloud material, then the disk wind, and finally the stellar wind (Table 2). The shock driven into the cloud is too slow to heat gas up to X-ray emitting temperatures, but large quantities of cloud material are ablated by the outflowing disk wind and mixed into this hotter flow (note that the cloud material does not directly mass-load the stellar wind - Fig. 3 shows that it is the disk wind which does this). This process heats the cloud material to temperatures where (soft) X-rays are emitted. This process of "mass-loading" the outflowing disk wind creates densities which are typically two orders of magnitude higher than the shocked stellar wind at comparable heights above the disk plane. However, the difference between the *attenuated* luminosities of the cloud and stellar wind components is very small ($L_{\mathrm{att_C}} = 8 \times 10^{28}$ and $L_{\mathrm{att_S}} = 7 \times 10^{28}\,\mathrm{erg\,s^{-1}}$, respectively). The explanation is that the stellar wind emission is harder and extends to higher energies, and is less affected by attenuation. In contrast, the cloud material, which is heated to lower temperatures, emits prolifically at low energies and has a much higher intrinsic luminosity, but its emission is subject to considerable attenuation at $E \lesssim 1$ keV. Examining the attenuated spectrum at $i = 60^\circ$ (Fig. 4), we find that the stellar wind material dominates the emission at $E \gtrsim 4$ keV, with comparable contributions from the winds and cloud material below this energy.

The observed model X-ray emission for $i = 60^\circ$ shows variability on timescales of order a few hundred years (Fig. 5). The total emission initially rises after the stellar and disk winds are switched on and a reverse shock is allowed to develop. There are then quasi-periodic oscillations, with noticeable dips at $t \simeq 500, 1000, 1300$, and 1700 yrs. The fluctuation in the total emission approximately follows

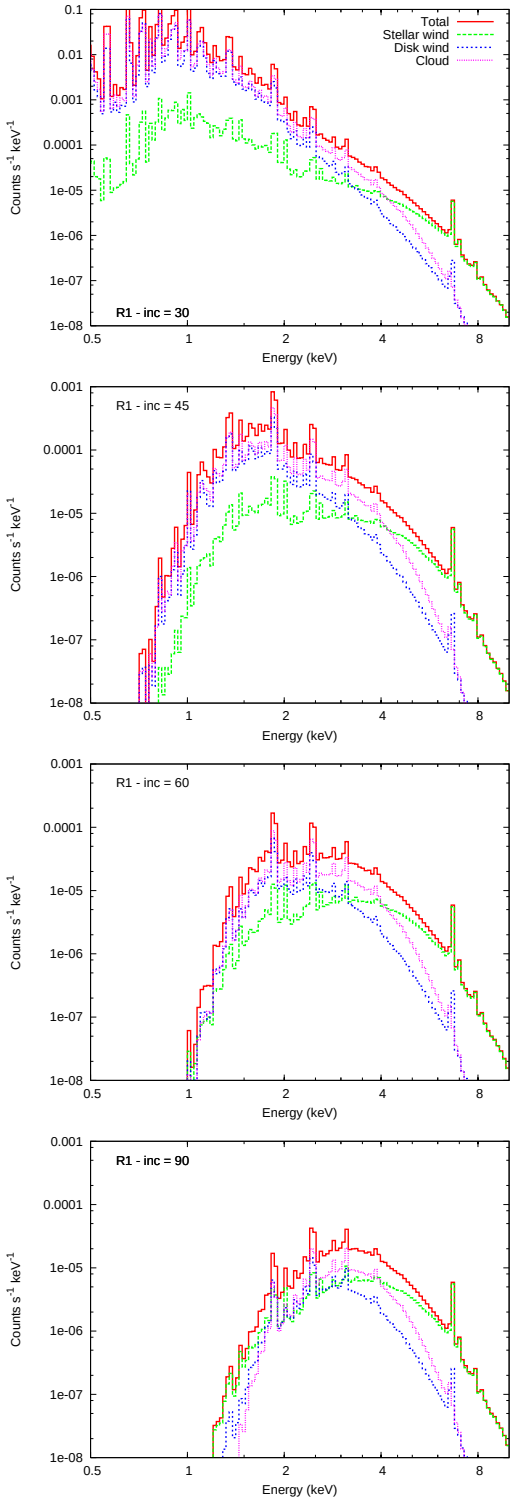

Figure 4. Attenuated 0.5-10 keV X-ray spectra for model R1 at various inclination angles. From top to bottom: $i = 30, 45, 60$, and 90°. The total (red), stellar wind (green), disk wind (blue), and heated cloud material (pink) emission are shown. All spectra were calculated at $t = 1000$ yr and have been convolved with the *Chandra* effective area. Note the difference in scale in the top panel.

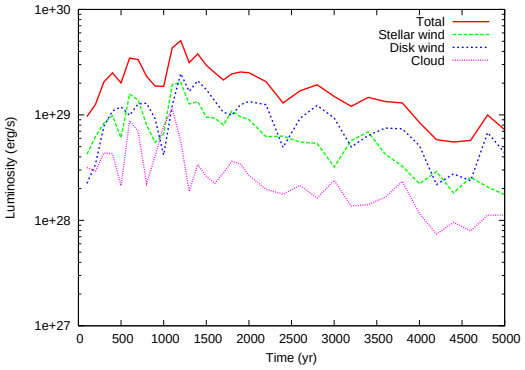

Figure 5. Attenuated 0.1-10 keV lightcurve for model R1 with $i = 60°$. The lightcurves of the separate emission components (stellar wind, disk wind, cloud) are also plotted.

the behaviour of the emission from the stellar wind. Some features are due to the disk wind luminosity, which is sometimes the dominant emitter. Fluctuations in both of these emission components is strongly related to the position of the reverse shock. At $t = 500$ yr the distance of the reverse shock from the star increases, and a reduction of the stellar wind luminosity occurs. Similarly, the maximum total luminosity occurs at $t = 1200$ yr, in conjunction with a minimum in the distance of the reverse shock from the star and a shape which results in more stellar wind material being shocked to the highest temperatures (Fig. 3). The variability in the observed emission is a general feature for all the simulations and complicates comparisons between the different model results. In simulation R1 the cavity has reached an approximate steady state and therefore the emission averaged over 500 or 1000 yrs should remain roughly constant. At $t = 1200$ yr a clump of disk wind is driven into the stellar wind by turbulent mixing (Fig. 3). Such mixing boosts the observed emission of both winds by heating the cooler disk wind and increasing the emission measure of the stellar wind. However, the bulk of the emission still originates from close to the reverse shock. The temperature of the stellar wind gas is also increased as it impacts the clumps and additional shocks are produced. At $t > 2000$ yr the attenuated luminosity appears to steadily decrease and the amplitude of the fluctuations seem reduced. This suggests that the variability at $t < 2000$ yr may be related to an initial evolutionary stage and thus to the initial conditions. Whether the variability to the observed emission will continue on longer timescales (i.e 10^5 yrs) is not clear as it depends on the postshock gas pressure. The luminosity of the cloud material follows the morphology of the winds, which suggests the magnitude and variability of this emission is related to the activities of the winds.

The visual extinction to a deeply embedded star relates to the column density along that line-of-sight. To allow comparison between our calculated column densities and observationally determined visual exctinctions, $A_{\rm v}$'s, we note the simple conversion factor $A_{\rm v} = N_{\rm H}/(1.9 \times 10^{21}\ {\rm cm}^{-2})$ mag (e.g. Cox 2000). One method of observationally determining the optical depth to the MYSO is to use the 9.7 μm Silicate feature (Crapsi et al. 2008). For the simulations, a good approximation is the column density to the star, $N_{\rm H-star}$ (i.e. the grid origin). Comparing this value to the emission weighted column (EWC), $N_{\rm EWC} = \Sigma N_{\rm Hc} L_{\rm intTc} / \Sigma L_{\rm intTc}$ (e.g. Parkin & Pittard 2008), where the index c indicates the column and luminosity from each cell on the hydrodynamic grid and the summation is over all cells, shows that the column density to regions with large intrinsic X-ray emission is significantly higher than that to the star (Table 2). This is mainly due to lines-of-sight to the X-ray emitting plasma in the receding lobe having longer path lengths and/or passing through denser material. For an inclination angle of $i = 60°$, the majority of the absorbing column is through the first ~ 2000 au of cloud gas beyond the cavity wall with a large fraction due to the layer of compressed cloud material which lines the cavity wall.

3.1.2 Inclination angle dependence of the observed X-ray emission

The attenuation of the emission is viewing angle dependent. When the inclination angle is $i = 30°$ the majority of lines-of-sight to X-ray emitting plasma avoid the densest cloud material close to the equatorial plane. This results in a lower $N_{\rm H-star}$ and significantly brighter spectrum at $E \lesssim 4$ keV than at $i = 60°$ (Fig. 4). At $E \gtrsim 4$ keV the harder stellar wind component dominates the spectrum. The disk wind and heated cloud material contribute the majority of the X-ray emission, with little difference between the two ($L_{\rm att_D} = 1.24 \times 10^{31}\,{\rm erg\,s^{-1}}$ and $L_{\rm att_C} = 1.61 \times 10^{31}\,{\rm erg\,s^{-1}}$, respectively). The total attenuated luminosity ($L_{\rm att_T} = 2.88 \times 10^{31}\ {\rm erg\,s^{-1}}$), and the integrated 0.1-10 keV count rate ($\eta \simeq 30\ {\rm ks^{-1}}$) are two orders of magnitude higher than observationally detected count rates.

When $i = 45°$, the majority of the X-ray emitting plasma is viewed through the cloud material. The column densities have increased relative to $i = 30°$ as now the line-of-sight to the star and to the regions with highest intrinsic emission must pass through sections of higher density, compressed cloud material. Examining the spectrum (Fig. 4) the turnover energy is now at $E \simeq 1.5$ keV. This is an increase relative to the $i = 30°$ case which illustrates the higher attenuation to the X-ray emission from disk wind and cloud material. At energies $E \gtrsim 4$ keV the spectrum has not changed significantly. $L_{\rm att_T}$ and η are now more in line with X-ray observations of massive star forming regions (e.g. Kohno et al. 2002; Preibisch et al. 2002; Giardino et al. 2004). Increasing the inclination angle further to $i = 60°$ results in a slight rise in $N_{\rm H-star}$, $N_{\rm EWC}$, and the turnover energy of the spectrum. Similarly, $L_{\rm att_T}$ and η decrease.

The maximum column densities are attained when viewing the system edge-on (i.e. $i = 90°$). It is interesting to note that the column to the star is now greater than the EWC, which indicates that for this viewing angle the column to the spatially extended (few thousand au) distribution of X-ray emitting plasma is lower than that to the star. Unlike the lower inclination angle calculations, emission below $E \lesssim 2$ keV is now observed from both lobes of the cavity. Also, the stellar wind material, which has the lowest intrinsic luminosity, now provides the largest contribution to $L_{\rm att_T}$. The spectrum above $E \sim 2$ keV remains roughly similar. We note that for inclination angles where the line-of-sight to the X-ray emitting plasma passes through the cloud ma-

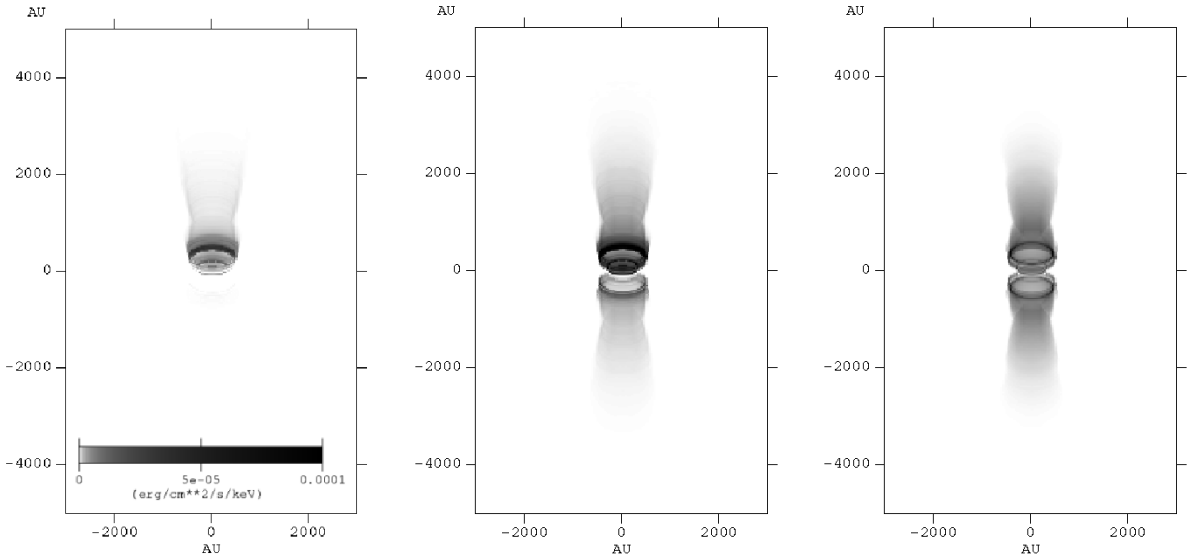

Figure 6. Broadband images of the attenuated X-ray emission from model R1 at $t = 1000$ yr, an inclination angle of $i = 60°$, a distance of 1 kpc, and in the energy bands 1-2 (left panel), 2-4 (middle panel) and 4-10 keV (right panel).

terial (i.e. $i \gtrsim 45°$ when $\omega \simeq 30°$), emission above $E \sim 4$ keV is mainly contributed by the shocked stellar wind.

The inclination angle dependence of the observed emission shows that there is a narrow range of angles where the count rate exceeds the *Chandra* X-ray detections.

3.1.3 Synthetic X-ray images

The raytracing code can produce synthetic broadband X-ray images which allow us to identify where different energy X-rays preferentially originate from. For simulation R1 at $i = 60°$, we see that the observable X-ray emission in the 1-2, 2-4, and 4-10 keV bands originates from similar regions of the cavity (Fig. 6). A peak in the intensity in the three bands originates near the reverse shock, and is mainly generated by shocked stellar and disk wind material (Fig. 4). Emission extending in the polar direction traces the boundary between the hot shocked stellar wind, and the cooler, higher density disk wind.

Examining Fig. 3 shows that the region of the cavity close to the pole is filled by hot shocked stellar wind. This gas emits the majority of the emission above $E \simeq 4$ keV (Fig. 4). The tower of emission visible in the 4-10 keV image in Fig. 6 therefore traces the stellar wind, with the shocked cloud emission in this energy band originating from the base of the cavity wall. The peak in intensity in all three bands occurs at the waist of the reverse shock, where there is a combined maximum in temperature and density. Examining the spectrum in the $E = 2 - 4$ keV energy range shows that this emission is from shocked disk wind and cloud material, which suggests it originates from the $T \sim 10^{6.5}$ K gas at $z = r \simeq 0.5 \times 10^{16}$ cm. Interestingly, both the preceding and receding lobes are observable in the 2-4 and 4-10 keV bands, which signifies the lessening influence of attenuation as the photon energy increases.

Importantly the spatial extents of the emission in all three energy bands (1-2, 2-4, and 4-10 keV) are just below the resolution limit of *Chandra* ($\sim 0.5''$) and so this model is consistent with the unresolved nature of real MYSOs. However, this finding is not true for all of our models which allows us to place constraints on some of the key model parameters.

3.2 Variation with mass inflow/outflow rates

The velocities of the inflowing and outflowing gas in the simulations are supersonic. As such, the morphology of the evolving cavity is strongly dependent on the ratio of the inflow and outflow ram pressure, which is directly proportional to the mass flow rates. There are a multitude of possible models with identical ram pressure ratios, but producing vastly different observable X-ray emission characteristics. Since optically thin bremsstrahlung emission has a density squared dependence (the emissivity $\propto n^2$), an increase in the mass-loss rates can have a considerable impact on the observed flux. However, an increase in the emission from cloud material due to an increase in $\dot{M}_{\rm infall}$ may be countered by an accompanying increase in attenuation. The degree of absorption is dependent on the column density, which is largely due to the cold cloud material, and therefore is directly proportional to the mass infall rate ($N_{\rm H} \propto \dot{M}_{\rm infall}$).

Decreasing the mass infall rate reduces the ram pressure of the infall. In model R2 the mass infall rate is halved to $\dot{M}_{\rm infall} = 1 \times 10^{-4}\,{\rm M}_\odot\,{\rm yr}^{-1}$. This results in less resistance to the outflows and subsequent expansion of the cavity. The cavity wall is hence wider at the base at an equivalent time. Also, the reverse shock is positioned at a greater distance from the star, and the enclosed region appears more elongated in the z-direction. Apart from the afore-mentioned differences we note that simulations R2 and R1 show similar evolution. As expected, $N_{\rm H-star}$ and $N_{\rm EWC}$ decrease by roughly a factor of two, consistent with the decrease in $\dot{M}_{\rm infall}$. There is a slight increase in $L_{\rm int_T}$ but $L_{\rm att_T}$ and η increase by factors of 2 and 3.5 respectively. Compared to model R1, the spectrum for model R2 (Fig. 7) shows higher flux at $E \lesssim 4$ keV and a softer spectrum above this en-

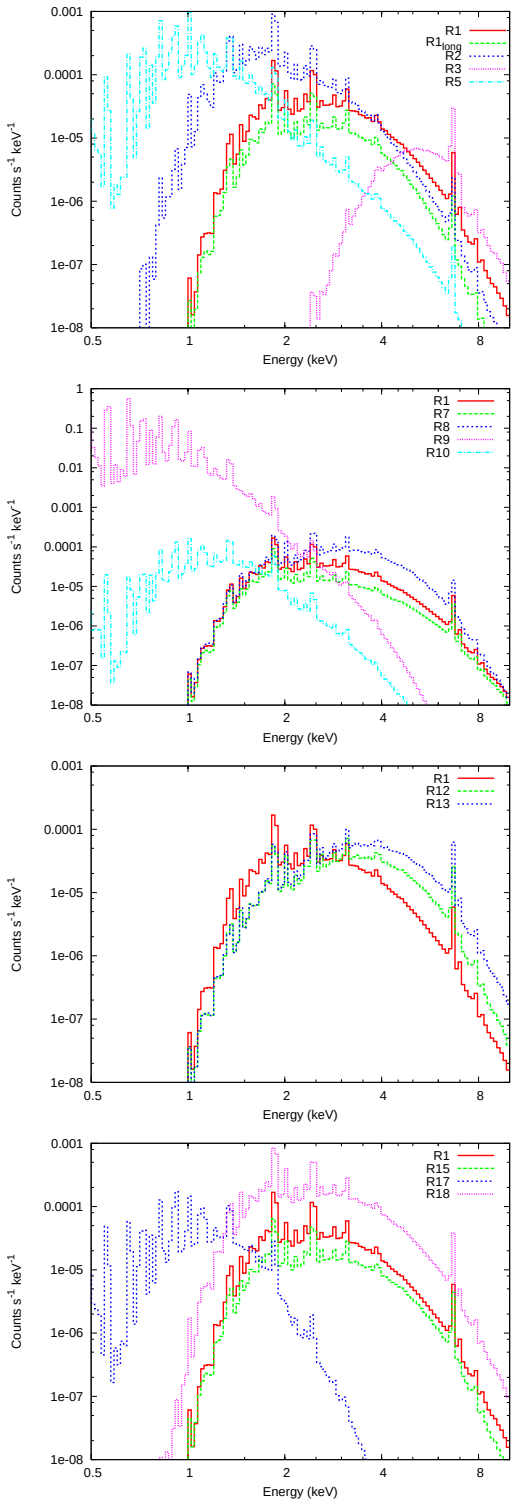

Figure 7. Total attenuated 0.5-10 keV spectra for simulations. The top panel shows R1, R1$_{\rm long}$, R2, R3, R5, the upper middle panel shows R1, R7, R8, R9, R10, the lower middle panel shows R1, R12, R13, and the lower panel shows R1, R15, R17, R18. All spectra were calculated at a time of $t = 1000$ yr (except models R1$_{\rm long}$ which was at $t = 5000$ yr, and R3 which was at t =500 yrs), using an inclination angle, $i = 60°$, and have been convolved with the *Chandra* effective area. Note the difference in scale in the upper middle panel.

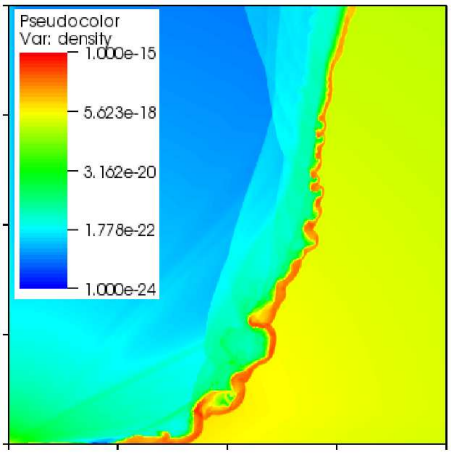

Figure 8. Density snapshot taken from model R4 at $t = 2000$ yr. The tick marks on the axis correspond to a distance of 10^{16} cm.

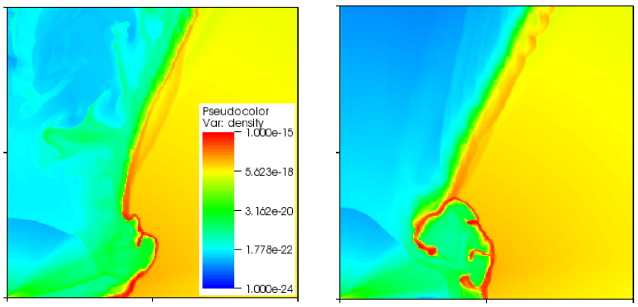

Figure 9. Density snapshots taken from model R7 at t =1700 (left) and 2000 yrs (right). The tick marks on the axis correspond to a distance of 10^{16} cm.

ergy which is linked to the differences in the position of the reverse shock.

If the mass infall rate is increased the ram pressure of the infalling material increases in direct proportion and the outflowing winds encounter more resistance to their expansion. In model R3 the reverse shock is pushed closer to the star by the increased mass infall rate, and the cavity now closes up over the star. At $t = 500$ yr the infall has begun to obstruct some of the outflow, and by $t = 900$ yrs the outflow has been fully constricted. Table 2 contains X-ray luminosities at $t = 500$ yr, before the cavity closes up (once closed the X-ray emission in our model becomes zero). Examining Table 2, we find that $N_{\rm H-star}$ and $N_{\rm EWC}$ have increased, and the $L_{\rm att}$'s and η's have decreased for R3 relative to R1. Note that $L_{\rm intC}$, increases considerably with $\dot{M}_{\rm infall}$, as the density, and thus the emission measure of this material, increases. However, the increasing attenuation with $\dot{M}_{\rm infall}$ removes more and more of the soft X-ray emission, so that the observed emission becomes increasingly hard (see Fig. 7). Model R3 shows that there is a delicate hydrodynamic balance between the infall and outflow, and large contrasts between these parameters can result in vastly different cavity evolution.

Confinement of a wind was discussed in the context of T-Tauri stars by Chevalier (1983), where the infall ram pressure can suppress the expansion of a wind into the sur-

rounding envelope. We have a similar situation, albeit more complicated by the anisotropic outflow. The wind at the base of the cavity may have a higher ram pressure than the stellar wind towards the pole of the cavity (as in model R3), which may ultimately lead to confinement at the poles but expansion at the base. Note also that the simulations we have performed only consider hydrodynamics, whereas a number of physical processes may in reality prevent a cavity from closing up. Magnetic fields may play an important role in controlling the dynamics of the infalling envelope (e.g. Banerjee & Pudritz 2007), or the radiation pressure may halt the inflow (i.e. Krumholz et al. 2005). However, it is clear that within the context of our model, the parameters for a slowly expanding cavity lie within a narrow range.

In model R4 the mass-loss rate of the stellar wind is increased to $1 \times 10^{-6}\,\mathrm{M_\odot\,yr^{-1}}$. The boundary between the inflowing and outflowing gas is likely to be subject to dynamical shear instabilities. Unlike in R1, such instabilities can be seen forming in the lower part of the cavity wall after $t \sim 500$ yr, with prominent structure visible at $t = 2000$ yrs (Fig. 8). A common feature in the simulations where these instabilities are noticeable (R4, R5, R9, R14, R15, and R18) is that the disk wind is compressed into a thin layer along the cavity wall. The timescale for KH instabilities to grow is $\propto (\rho_1 + \rho_2)/\sqrt{\rho_1\rho_2}$, and the enhanced disk wind density along the cavity wall results in an increased growth rate for these instabilities. In addition to this, in the afore-mentioned simulations the cavity wall becomes curved at the base due to the action of the winds (except in R18 where the cavity is initially curved). As such, the shocked winds have a small grazing angle against the base of the cavity wall and the velocity difference across the shear boundary is higher. These instabilities cause the initially smooth cavity wall to become deformed, and in the more severe cases these deformations grow into jagged features. As these features protrude into the winds clumps of cloud material are stripped away and then ablated. In model R1, we see disk wind material mixing into stellar material (see Fig. 3), while in model R4 (Fig. 8) we see cloud material mixing into disk wind material. Such mixing can cause the disk wind to become more confined to the lower regions of the simulation domain, and no longer border the entire cavity wall. Also of note in model R4 is that the wind-driven expansion of the cavity opposes the infall and it is conceivable that at $t > 2000$ yr the flow of cloud material onto the disk plane will be halted and the envelope will be completely destroyed by the winds. The increase in $\dot{M}_\mathrm{S}$ results in an increase in the L_att's and η.

In model R5 the ratio of the inflow/outflow ram pressures is the same as in R4, but $\dot{M}_\mathrm{infall}$, $\dot{M}_\mathrm{S}$, and $\dot{M}_\mathrm{D}$ are all ten times lower. Nevertheless, the evolution of the cavity and the position and shape of the reverse shock are almost identical between R4 and R5, as one would expect. The intrinsic emission decreases by a factor of 100, as expected ($EM \propto \dot{M}^2$). However, η only decreases by a factor of ~ 2, since the attenuation is also vastly reduced. Comparing the spectra (Fig. 7) we see that in the 4-10 keV band the spectral slope is almost identical, yet for R5 the count rate in this band is roughly a factor of 100 lower. Therefore, although count rates consistent with observations can still be attained when the mass flow rates are scaled down, the much softer observed spectrum places constraints on the outflow, and consequently the inflow, parameters.

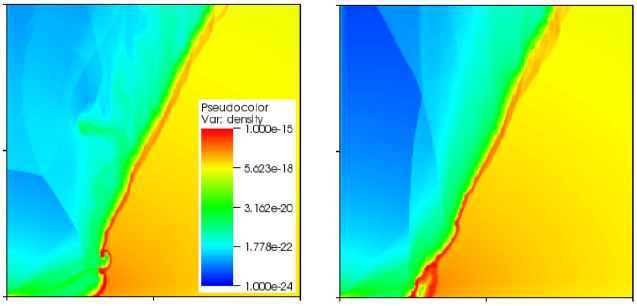

Figure 10. Density snapshots taken from model R8 at $t = 600$ (left) and 900 yrs (right). The tick marks on the axis correspond to a distance of 10^{16} cm.

In R6 the mass-loss rate of the disk wind is increased by a factor of 3 from R1 to $\dot{M}_\mathrm{D} = 3 \times 10^{-6}\,\mathrm{M_\odot\,yr^{-1}}$. If $\dot{M}_\mathrm{infall}$ is kept at $2 \times 10^{-4}\,\mathrm{M_\odot\,yr^{-1}}$ the disk wind drives a hole into the base of the cavity wall. To prevent this occurence $\dot{M}_\mathrm{infall}$ is increased to $1 \times 10^{-3}\,\mathrm{M_\odot\,yr^{-1}}$. The resulting cavity evolution is somewhat similar to that of R1. However, the fact that $\dot{M}_\mathrm{infall}$ has been increased to stabilise the cavity evolution brings an accompanying increase in the column densities so that the attenuated luminosity is actually lower than that from model R1. Compared to model R3 (which has identical parameters except for a lower value of $\dot{M}_\mathrm{D}$) we see that the higher value of $\dot{M}_\mathrm{D}$ prevents the infall from totally overwhelming the outflow.

Reducing the mass-loss rate of the stellar wind (R7) leads to major differences in the cavity evolution. The pressure applied to the cavity wall by the winds as a function of polar angle now differs more than in model R1 (there is now a factor of 20 variation in $\dot{M}_\theta$). Whereas the stellar wind previously had sufficient ram pressure to hold back the infalling cloud material, the cavity now begins to close up above the star. At $t \simeq 1500$ yrs the disk wind begins to cut into the base of the cavity wall, and the bubble formed continues to increase in size for the duration of the simulation (Fig. 9). By $t = 2000$ yrs a limb of cloud material is extending towards the star. Further analysis shows that by $t = 2300$ yrs this material breaks away from the cavity wall and obstructs the outflowing winds close to the star.

3.3 Variation with wind speeds

The preshock velocity dictates the postshock gas temperature ($T \propto v^2$). Hotter gas emits higher energy X-rays, and an increase or reduction in the wind speeds will affect the hardness of the resulting spectrum.

In model R8 the stellar wind velocity is increased to $v_\mathrm{S} = 3000\ \mathrm{kms^{-1}}$. The shocked stellar wind now reaches $T \gtrsim 10^8$ K. The equatorial flow appears to be more powerful and drives a small, short-lived hole into the base of the cavity wall (Fig. 10). This is unexpected as it is the ram pressure of the stellar wind which has been increased. However, it seems that the total pressure near the equatorial plane is enhanced by an increase in the thermal pressure adjacent to the reverse shock. Subsequently, the cloud material then collapses (see Fig. 10) and fills the hole, after which the cavity settles into a steady state similar to that of model R1. The higher ram pressure of the stellar wind increases the

Table 2. Column densities (columns 3 and 4), intrinsic (int) and attenuated (att) 0.1-10 keV X-ray luminosities (columns 5-8 and 9-12, respectively), and integrated count rates (column 13) from raytraced emission calculations. The stellar wind (S), disc wind (D), and cloud material (C) contributions to the total (T) luminosity are shown. The integrated 0.1-10 keV count rate, η, was calculated using the *Chandra* effective area (see § 2.5). Luminosities are in 10^{31} erg s^{-1}, and count rates are in ks^{-1}. $N_{\rm H-star}$ and $N_{\rm EWC}$ are the column density measured to the star and the emission weighted column respectively, both of which are in 10^{23} cm^{-2}. The raytracing calculations were performed with an inclination angle of $i = 60°$, except R1$_{30}$, R1$_{45}$, and R1$_{90}$ which were calculated using inclination angles of 0, 30, 45, and 90° respectively. All calculations were performed on simulations at $t = 1000$ yr, except R1$_{\rm long}$ and R3 which were calculated at 5000 and 500 yrs, respectively.

Model	Comment	$N_{\rm H-star}$	$N_{\rm EWC}$	$\rm L_{int_T}$	$\rm L_{int_S}$	$\rm L_{int_D}$	$\rm L_{int_C}$	$\rm L_{att_T}$	$\rm L_{att_S}$	$\rm L_{att_D}$	$\rm L_{att_C}$	η
R1		2.47	6.09	370	0.500	43.1	330	0.019	0.007	0.004	0.008	0.11
R1$_{30}$		0.44	5.42	370	0.500	43.1	330	2.88	0.035	1.24	1.61	30
R1$_{45}$		3.11	6.21	370	0.500	43.1	330	0.040	0.008	0.012	0.020	0.35
R1$_{90}$		9.66	7.03	370	0.500	43.1	330	0.012	0.006	0.002	0.004	0.05
R1$_{\rm long}$	longer run	2.40	5.54	186	0.221	26.1	157	0.007	0.002	0.004	0.001	0.05
R2	$\dot{M}_{\rm infall} \downarrow$	0.99	3.19	436	0.313	32.2	404	0.040	0.005	0.021	0.014	0.37
R3	$\dot{M}_{\rm infall} \uparrow$	16.7	46.4	3070	0.596	27.7	3050	0.014	0.002	0.005	0.007	0.02
R4	$\dot{M}_{\rm S} \uparrow$	1.92	3.46	220	1.39	33.4	185	0.071	0.043	0.015	0.012	0.41
R5	R4 with $\dot{M}$'s $\downarrow$	0.25	0.37	2.48	0.11	0.22	2.16	0.016	0.002	0.006	0.008	0.23
R6	$\dot{M}_{\rm infall} \uparrow$, $\dot{M}_{\rm D} \uparrow$	16.9	46.6	6120	5.27	395	5720	0.008	0.007	7×10^{-4}	5×10^{-4}	0.02
R7	$\dot{M}_{\rm S} \downarrow$	2.47	6.39	390	0.470	44.1	345	0.009	0.005	0.002	0.002	0.05
R8	$v_{\rm S} \uparrow$	2.48	7.38	569	0.142	33.8	535	0.049	0.005	0.003	0.011	0.26
R9	$v_{\rm S} \downarrow$, $\dot{M}_{\rm S} \uparrow$	2.10	4.40	215	4.49	36.8	174	0.042	0.027	0.008	0.007	0.28
R10	B star	0.38	0.96	13.5	0.066	2.26	11.2	0.004	4×10^{-4}	7×10^{-4}	0.003	0.06
R11	$\theta_{\rm S} = 70°$	2.83	7.42	438	1.64	31.5	405	0.019	0.013	0.003	0.003	0.08
R12	$\theta_{\rm S} = 85°$, $\theta_{\rm D} = 89°$	3.00	9.15	526	2.41	6.93	516	0.030	0.017	0.002	0.012	0.12
R13	no disk wind	2.93	9.52	456	2.22	–	454	0.060	0.032	–	0.029	0.20
R14	$\omega = 5°$	2.41	6.66	318	0.253	27.8	290	0.051	0.011	0.016	0.024	0.30
R15	$\omega = 10°$	2.82	7.22	483	0.577	54.5	4.28	0.009	0.006	0.002	0.002	0.05
R16	$\omega = 45°$	2.14	6.40	219	0.219	23.8	195	0.018	0.004	0.012	0.002	0.12
R17	$\omega = 60°$	1.21	3.36	27.5	0.125	11.9	15.4	0.003	2×10^{-5}	3×10^{-4}	0.003	0.05
R18	$\beta = 2$	1.36	3.40	341	1.11	30.3	310	0.099	0.036	0.015	0.048	0.58
R19	$r_{\rm c} \downarrow$	2.86	7.42	754	0.378	45.2	708	0.025	0.006	0.009	0.010	0.14
R20	$r_{\rm c} \uparrow$	2.39	6.21	148	0.158	11.7	136	0.079	0.008	0.059	0.012	0.39

maximum distance of the reverse shock from the star, and its amplitude of oscillation. Increasing the stellar wind velocity causes the spectral hardness (Fig. 7) and the *Chandra* count rate, η, to increase. Interestingly, the X-ray emission from the disk wind and cloud material is now dominant at all energies. Whereas $L_{\rm att_S}$ and $L_{\rm att_C}$ were approximately equal in model R1, $L_{\rm att_C}$ is twice as high as $L_{\rm att_S}$ in model R8. This is likely a result of increased turbulent heating by the stellar wind. A decrease in $L_{\rm int_S}$ occurs because the reverse shock is further from the star, leading to a lower postshock density, and thus a lower emission measure.

Recent theoretical models of stellar evolution by Hosokawa & Omukai (2009) predict that for high accretion rates ($\sim 10^{-3}\,{\rm M_\odot\,yr^{-1}}$) the protostellar radius becomes very large. This results in a lower surface gravity for the protostar and consequently the stellar wind will be more like that of a supergiant (i.e. $v_{\rm S} \lesssim 1000$ km s^{-1}) than a main sequence O-star. Model R9 explores this scenario, where $\dot{M}_{\rm S} = \dot{M}_{\rm D} = 10^{-6}\,{\rm M_\odot\,yr^{-1}}$ and $v_{\rm S} = 1000\,{\rm km\,s^{-1}}$. With a greater ram pressure in the stellar wind compared to model R1, the cavity does not initially narrow at the top of the grid. The postshock stellar wind has a lower temperature ($T \sim 10^{6.5}$ K) because of the lower preshock velocity. The position of the reverse shock is much further from the star ($z \sim 4 \times 10^{16}$ cm), and this distance increases as the simulation progresses. The column densities are lower (Table 2), likely due to the greater height of the reverse shock (and thus the postshock gas) above the disk plane, and thus the reduced path length through cloud material for lines-of-sight. The spectrum is very different from that of R1 and is clearly a lot softer (Fig. 7). The stellar wind component now dominates the observed emission at $E \sim 1$ keV as the denser stellar wind increases the emission measure. The synthetic X-ray images show the approaching lobe to be fully illuminated by X-ray emission, unlike the narrow tower seen for R1 in Fig. 6, with the intensity peaks in the 1-2, 2-4 and 4-10 keV bands being $\gtrsim 1''$ in extent (see Fig. 11).

Comparing models R4 and R9 gives insight into the effects of reducing the stellar wind speed, $v_{\rm S}$, with all other parameters kept the same. In a similar respect to models R1 and R8, the reduction in $v_{\rm S}$ causes the reverse shock to be closer to the star, and the postshock stellar wind tempera-

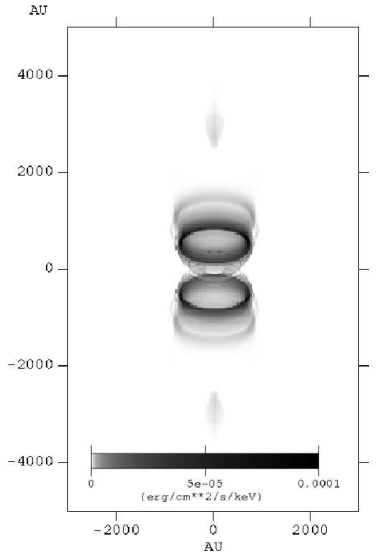

Figure 11. Broadband image of the attenuated X-ray emission for model R9 at an inclination angle of $i = 60°$, a distance of 1 kpc, and in the 4-10 keV energy band.

ture to be lower ($\sim 10^{6.5}$ K). Column densities are slightly higher for model R9. The $L_{\rm int}$'s are very similar, yet the $L_{\rm att}$'s and η are slightly lower. Comparison of the spectra shows that for model R9 the flux level is slightly lower and the spectral slope at $E \gtrsim 4$ keV is slightly softer than model R4.

A number of known objects possessing outflow cavities where X-ray emission has been detected have been inferred as early B-type stars. These stars will have lower terminal wind speeds and mass-loss rates than the O-type star used as our fiducial model. In model R10 we use stellar wind parameters corresponding to a B1V star (Prinja 1989). Consequently, the mass infall rate must be scaled down to produce a similar ram pressure balance to that of model R1. The evolution of the cavity is qualitatively similar to model R1. However, the different ram pressures of the inflow and outflow produces more vigourous ablation of the base of the cavity wall than in model R1. The reduced stellar wind velocity results in a lower maximum postshock gas temperature, which in-turn reduces the amount of hard X-ray emission. The column densities are significantly reduced compared to model R1, and are in agreement with observationally determined values for embedded early B-type stars (e.g. Preibisch et al. 2002). The spectrum is much softer now (Fig. 7).

3.4 Variation with wind geometry

Varying the wind geometry affects the contributions to the total emission from the different components, and changes the cavity evolution. For instance, increasing the opening angle of the stellar wind provides more stellar wind material, and less disk wind material. If the ram pressure of the stellar wind is much greater than that from the disk wind the latter may be channelled into an equatorial outflow, as found in model R8. To explore the consequences of different wind geometries we have calculated models R11, R12, and R13 (see Table 1).

As the opening angle of the stellar wind is increased (c.f. models R1, R11, and R12), and that of the disk wind decreased, the thickness of the disk wind layer along the cavity wall becomes thinner due to the reduced amount of disk wind being injected. The evolution of the cavity remains similar to that of R1, although the cavity wall is now more curved towards the base. The base of the cavity wall is closer to the star because the ram pressure of the outflow close to the disk plane is now reduced. The aspect ratio of the region of unshocked winds increases as the reverse shock moves to smaller r. The value of η does not vary much from that calculated for R1 though the observed spectrum is harder (see the spectrum from model R12 in Fig. 7).

To explore the effect of having a spherical outflow we have constructed model R13, which is equivalent to R1 except with no disk wind. We find that compared to model R1 there is a definite hardening with more X-ray emission at $E \gtrsim 4$ keV (Fig. 7), which is expected as there is now more high speed material in the outflow. There is also an enhancement in $L_{\rm att_C}$ due to heating of this gas to hotter X-ray emitting temperatures by direct contact with, and thus greater turbulent heating from, the stellar wind. The value of η remains in agreement with observationally detected values for MYSOs. Interestingly, this shows that X-ray emission can be generated from the wind-cavity interaction in the absence of a disk wind, which means this mechanism could be applicable to more evolved protostars as well.

3.5 Variation with cavity opening angle

The angle that the outflow makes with the cavity wall affects the rate at which kinetic energy in the preshock gas is transferred into thermal energy in the shocked gas. Also, the pressure of the shocked gas is affected by the degree of confinement provided by the cavity wall. Keeping all other parameters the same, a narrow cavity leads to higher gas pressures than a wider cavity. This has implications for the wind-driven expansion of the cavity and the position and shape of the reverse shock. To explore these effects further models R14-R17 have been performed.

When ω is reduced relative to R1 (as in models R14 and R15) the cavity is initially narrower, and the postshock thermal pressure higher. This results in a rapid expansion of the cavity in order to balance the pressure across the cavity wall. In model R14 the cavity seems to have relaxed by $t = 1000$ yrs, whereas in model R15 expansion still appears to be ongoing at this time. By the end of both simulations the cavity has a roughly curved shape. The rapid expansion of the cavity wall away from the star causes turbulent mixing and fluctuations in the shape and position of the reverse shock. Instabilities form in the cavity wall as the less dense outflow collides with the more dense inflow, causing a combination of KH, Rayleigh-Taylor, and Richtmeyer-Meshkov instabilities. The column densities relative to those from model R1 are higher because of the longer path lengths for lines-of-sight through cloud material and because the initial cavity is cut into the cloud closer to the star. The conclusion that the values of η and $L_{\rm att_T}$ are higher for smaller initial cavity opening angles appears to only be true for model R14. However, the lower η at $t = 1000$ yr resides at a minimum in the lightcurve for model R15. The spectrum remains similar to

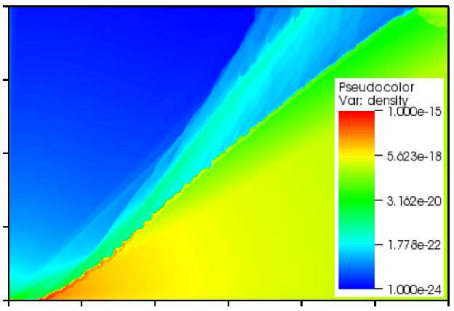

Figure 12. Density snapshot taken from model R17 at t = 1000 yr. The tick marks on the axis correspond to a distance of 10^{16} cm.

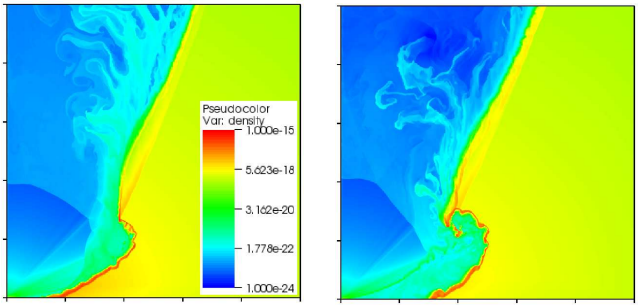

Figure 13. Density snapshots taken from model R18 at $t = 1400$ (left) and 2000 yrs (right). The tick marks on the axis correspond to a distance of 10^{16} cm.

that of R1 at $E \lesssim 2$ keV, and shows more emission above this energy (Fig. 7).

In models R16 and R17 the cavity half opening angle is increased compared to model R1. For $\omega = 45°$ (R16), a reverse shock is still generated close to the star which encloses the unshocked winds. Interestingly, when $\omega = 60°$ (R17) this no longer happens (see Fig. 12). This is the result of a shallow grazing angle for the wind-cavity collision. The shocked gas now only resides along the cavity wall, and the maximum temperatures reached are $T \sim 10^{6.5}$ K. The disk wind forms a layer along the cavity wall. On the interior side of the cavity it is bordered by the shocked stellar wind. Column densities and the intrinsic and attenuated emission decrease with increasing ω. When there is no reverse shock (close to the star) η drops significantly and the spectrum becomes much softer (see the spectrum from model R17 in Fig. 7).

3.6 Variation with cavity curve

The shape of the cavity may not initially be conical, as has been assumed in simulations R1-R17 and R19-20. In fact, some observations of cavities around MYSOs show them to be more parabolic in shape. It is unclear whether an initially conical outflow cavity evolves to become more curved. Such evolution could be driven by the action of the outflowing winds (as in R1), or by changes to the mechanism that drives the outflow causing the resulting cavity to be curved at the base. The initial curvature of the cavity wall is controlled by the exponent β in Eq. 8. In model R18 we adopted $\beta = 2$, i.e. a parabolic cavity. A reverse shock is still formed, although it occurs at a greater distance from the star, and with a different shape than that seen in model R1 (Fig. 13). The reverse shock can be divided into two parts. The upper part (which spans polar angles $0 < \theta \lesssim 60°$) is very clearly normal to the stellar wind, which leads to postshock gas at very high ($\sim 10^8$ K) temperatures and hard and luminous X-ray emission (Fig. 7). The lower part, in contrast, is very oblique to the disk wind, and leads to much cooler postshock temperatures. For the duration of the simulation infalling cloud material can still reach the disk plane. However, by $t = 2000$ yr this accretion flow has halted due to the pocket of hot rarefied disk wind gas which sweeps up the cloud material and drives it into the equatorial outflow cavity (Fig. 13). Also noticeable by the end of the simulation is that the disk wind is confined to the equatorial outflow bubble, and the larger cavity towards the pole is filled with turbulent shocked stellar wind gas.

In conclusion, introducing curvature into the cavity wall at the start of the simulation does not prevent integrated count rates in approximate agreement with observations from being produced and the spectrum appears largely similar, though a factor of 3 or so brighter (Fig. 7). Curvature produced by a previous outflow may be erased as the winds carve into the cavity wall.

3.7 Variation with centrifugal radius

The spherically averaged density goes as $\rho \propto r^{-1/4}$ within r_c, and $\rho \propto r^{-3/2}$ at distances greater than r_c. Therefore, changing r_c affects the density distribution in the cloud.

In model R19, r_c is decreased to 0.8×10^{15} cm, and as such the density in the cloud material should be lower than that of model R1 at equivalent distances from the star. There is however little noticeable difference between the cavity evolution in this simulation and R1. There is a minor increase in $N_{\rm H-star}$ which is consistent with the cavity wall being slightly closer to the star for model R19. The increase in $N_{\rm EWC}$ is a result of the spatial distribution of the emission and the position of the reverse shock. The reverse shock is now closer to the star than in model R1, and as such there is more emission from the disk wind close to the base of the cavity wall. Lines-of-sight to this disk wind gas pass through the dense cloud gas close to the axis, resulting in higher column densities. However, in spite of this η is higher because of the enhancement to the emission measure brought about by the position of the reverse shock.

The value of r_c is increased to 6.0×10^{15} cm in simulation R20. The winds now excavate the base of the cavity wall more. This excavation proceeds in an unsteady manner, and results in more variation in the degree of mixing between the winds and the position of the reverse shock throughout the simulation than seen in model R1. These differences in the dynamics result in increased variability of the resulting emission; for model R1 the largest amplitude oscillations in the attenuated luminosities was a factor of ~ 2 (Fig. 5), whereas for model R20 there are oscillations of a factor of ~ 4. The spectrum at $t = 1000$ yrs represents the median for model R20.

Table 3. Model parameters (see also Table 1) and results for the candidate objects. The distances are taken from Schneider et al. (2006), Staude et al. (1982) and Racine (1968), and the inclination angles are from van der Tak et al. (2006), Solf & Carsenty (1982) and Alvarez et al. (2004a) for AFGL 2591, S106 IRS4, and Mon R2 IRS3 A, respectively. $N_{\rm H-star}$ and $N_{\rm EWC}$ are in units of 10^{23} cm^{-2}.

Model	D (kpc)	i (°)	$N_{\rm H-star}$	$N_{\rm EWC}$	η (ks^{-1})
S106	0.6	75	0.4	0.8	0.23
Mon R2	0.83	45	0.6	1.1	0.12
AFGL 2591	1.7	32	2.0	6.9	0.09

4 CANDIDATE OBJECTS

We compare our model against X-ray observations of three objects: S106 IRS4, Mon R2 IRS3 A, and AFGL 2591. Because of the low count rates spectral fits to these objects are relatively meaningless. Therefore we restrict our comparison to the integrated count rates and the generation of X-rays above 2 keV. We also examine whether the model flux falls below the detection limit (and is spatially unresolvable) when reasonable model parameters are used. We place the constraint on the model parameters that the cavity must be reasonably steady (i.e. the infall does not constrict the outflow at any point during the simulation) and the visual extinction agrees with observation. Therefore, the main free parameters are $\dot{M}_{\rm S}$ and $\dot{M}_{\rm infall}$ (as disk wind parameters were based on previous observational estimates).

4.1 S106 IRS4

S106, at a distance of 600±100 pc (Staude et al. 1982), is a massive star-forming region known for an extended bipolar HII region, which is illuminated by the $\gtrsim 15\,{\rm M}_\odot$ massive star S106 IRS4 (Felli et al. 1984). Schneider et al. (2002) find the observed morphology and kinematics in ^{12}CO and ^{13}CO 2→1 to be consistent with a cavity created by the radiation and ionized wind from S106 IRS4 sweeping up material from the cavity wall, marked by the two lobes of the HII region and at the extreme ends of the flow. They also find that the double-peak structure of the cloud breaks down and the emission merges into a more diffuse extended plateau at S106 IRS4, where the molecular emission traces the red-shifted component of the stellar wind hitting the backside of the cavity walls. Near-IR speckle observations by Alvarez et al. (2004b) show only a single unresolved source at the position of S106 IRS4. Solf & Carsenty (1982) used the kinematics of the bipolar nebula to deduce that the inclination angle of the system in the plane of the sky is $\sim 75°$.

To determine the input parameters for our model of S106 we calculated a series of models with various $\dot{M}_{\rm S}$, $\dot{M}_{\rm D}$, and $\dot{M}_{\rm infall}$, where we fixed i, $v_{\rm S}$, $v_{\rm D}$, and ω. A good match to the *Chandra* count rate and the visual extinction, $A_{\rm v}$, was found for one particular model, with parameters as noted in Table 1. From this model we calculate a count rate (Table 3) in agreement with the 0.30±0.11 ks^{-1} *Chandra* detection (Giardino et al. 2004). The $N_{\rm H-star}$ and $N_{\rm EWC}$ values correspond to visual extinctions of $A_{\rm v} = 22$ and 39 mag respectively, which are consistent with previously determined values (Giardino et al. 2004). The model parameters for the stellar wind terminal velocity and mass-loss rate are consistent with an early B-type star. For the disk wind, the terminal velocity was set to the previous estimate of $\simeq 350\,{\rm km\,s^{-1}}$ (Drew et al. 1993), whereas the mass-loss rate is roughly an order of magnitude lower than previously determined values of $1.6 - 1.8 \times 10^{-6}\,{\rm M_\odot\,yr^{-1}}$ (Felli et al. 1984; Hoare et al. 1994; Gibb & Hoare 2007). This difference may be due to wind clumping causing over-estimates in the mass-loss rate determinations from free-free emission. We note that amongst B-type stars, a mass-loss rate as high as $1.8 \times 10^{-6}\,{\rm M_\odot\,yr^{-1}}$ is consistent only with an evolved supergiant luminosity type, with main sequence stars having mass-loss rates typically two or more orders of magnitude lower (e.g. Prinja 1989).

4.2 Mon R2 IRS3 A

The general structure of the observable nebula around IRS3 A is clearly monopolar, which suggests IRS3 A is embedded in a disk or torus with bipolar cavities. Preibisch et al. (2002) obtained high resolution (75 mas = 62 au) near-infrared H and K band images of Mon R2 IRS 3 which show a close triple system surrounded by strong diffuse nebulosity and three additional infrared sources within 3" of the brightest object IRS3 A ($K \sim 7.9$, $M_* = 12 - 15\,{\rm M_\odot}$), which has not yet developed an HII region (Alvarez et al. 2004b). For a review of the Mon R2 star-forming region see Carpenter & Hodapp (2008). Preibisch et al. (2002) comment that the X-ray properties of IRS3 A and C cannot be explained by stellar wind models where the X-rays are generated at shocks inherent to the winds as the emission is much harder. This agrees with the comment by Kohno et al. (2002) that the observed plasma temperatures of $\gtrsim 4$ keV ($T \gtrsim 5 \times 10^7$ K) are ten times higher than plasma temperatures typical for early B-type main sequence stars. As has been shown in § 3, shock temperatures in a winds-cavity interaction can reach $\gtrsim 10^8$ K.

In model Mon R2 (Table 1) and the subsequent X-ray calculation we use values for $r_{\rm c}$, $r_{\rm cav}$, ω, and i determined by Alvarez et al. (2004a) from fits to observations with envelope radiative transfer models. The model count rate (Table 3) agrees with the *Chandra* value of 0.166±0.041 ks^{-1} determined by Preibisch et al. (2002). The stellar wind terminal velocity and mass-loss rate imply a late-O/early-B type central star. The mass infall rate for model Mon R2 is roughly a factor of 5 lower than that determined by Alvarez et al. (2004a). However, this difference is not surprising as the evolved state of the envelope in our model produces a dense layer of compressed cloud material along the cavity wall, which increases the column to the star. This feature is not present in envelope radiative transfer models, which typically assume a smooth density distribution. As such, to attain a visual extinction which agrees with the observations we must decrease the mass-infall rate.

4.3 AFGL 2591

The $\sim 16\,{\rm M_\odot}$ (van der Tak & Menten 2005) early B-type star AFGL 2591 sits at the centre of a powerful bipolar molecular outflow cavity orientated in the east-west direction (Lada et al. 1984; Mitchell et al. 1992). The central source is fully obscured in the optical and J band. The exis-

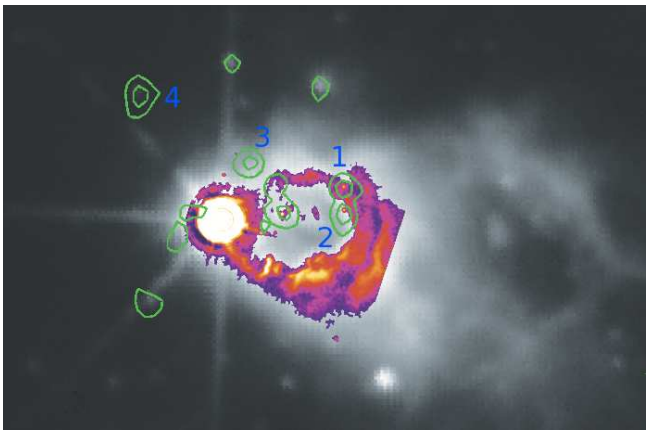

Figure 14. Near-infrared speckle interferometry from Preibisch et al. (2003) and contours from a *Chandra* X-ray image smoothed with a 1" gaussian super-imposed on the UKIDSS K band image of the AFGL 2591 region. The detected point-like sources noted in Table 4 are labelled.

Table 4. Detected point-like X-ray sources in the vicinity of AFGL2591. $\tilde{E}$ is the median photon energy from the source. The net counts have been background subtracted. $P_{\rm not}$ is the Poisson probability that the source is a chance coincidence of background photons—the "not-a-source" probability.

No.	RA (deg)	Dec (deg)	$\tilde{E}$ (keV)	Net counts	Signif. (σ)	$P_{\rm not}$
1	307.3508	40.1894	3.9	6.69	1.77	5.7e-8
2	307.3508	40.1888	3.2	6.71	1.77	3.3e-8
3	307.3554	40.1910	2.9	6.72	1.78	2.6e-8
4	307.3530	40.1898	4.3	5.72	1.59	6.6e-7

tence of a large-scale torus perpendicular to the outflow cavity is inferred from extended CS emission (Yamashita et al. 1987). Nebulous loops are clearly seen in the bispectrum speckle interferometry images of Preibisch et al. (2003), which are thought to mark the peripheries of outflow bubbles. When modelling high-resolution SO data, Benz et al. (2007) found the inclusion of X-ray emission (which may originate from outflow shocks) improved model fits.

AFGL 2591 was observed by *Chandra* on 2006 February 8 using the Advanced CCD Imaging Spectrometer (ACIS) S3 chip in very faint mode for an exposure time of 30.17 ks. Data were obtained from the *Chandra Data Archive*[3] and were processed in a standard way using the *Chandra* Interactive Analysis of Observations (CIAO, Fruscione et al. 2006) software version 4.1.1.

Point source detection was performed using the CIAO `wavdetect` task (Freeman et al. 2002) on the level 2 event file. The process works by correlating the dataset with a number of "Mexican Hat" wavelet functions at different spatial scales to search for correlations. This process was performed at a significance threshold of 10^{-5}, corresponding to less than 1 false source for the whole S3 field, and resulted in 4 sources detected in the vicinity of AFGL 2591 (Fig. 14 and Table 4) and 62 sources in the whole S3 field. The point sources are identified with stellar point sources in a deep UKIDSS K band image of the region illustrated in Fig. 14.

To correct for systematic errors in the Chandra aspect system (typically about 1 arcsec), we searched for near-IR counterparts from the UKIDSS (Lawrence et al. 2007) Galactic Plane Survey (Lucas et al. 2008) catalogue across the entire CCD and identified bright counterparts for 12 of the detected X-ray point sources. These counterparts were used to correct the *Chandra* coordinates and register them to the UKIDSS reference frame.

Source extraction was performed using ACIS Extract (AE, Broos et al. 2002), an IDL-based package developed for ACIS data processing. The procedures used in AE are described in **?** and **?**. Model point spread functions (PSFs) were constructed for each source together with contours which contain >90% of source events. The background was estimated locally for each source using circular annuli around their respective PSFs that avoided the PSFs of other nearby sources. From the background subtracted net counts, the median energy, source significance and the Poisson "not-a-source" probability were calculated for each source. The results, source positions, and characteristics are listed in Table 4. These sources are neighbouring low-mass stars and are not associated with the outflow from AFGL 2591.

AFGL 2591 was not detected as a point source, unlike S106 IRS4 and Mon R2 IRS3 A where the X-ray emission was unresolved. However, there is a tentative detection of diffuse emission (visible as the contours east of the central source in Fig. 14) with count rate of ~ 0.2 ks^{-1} from a circular region, centered on AFGL 2591 with radius $\sim 2.6''$, with a significance of 3.7 σ above the background level (determined using the method of Pease et al. 2006, which expresses the probability that the observed counts cannot be explained by Poissonian variations in the background and is different to the signal-to-noise ratio of the extracted signal). The origin of the observed emission is unclear and we interpret it as due to the interaction of the winds from the central object with the surrounding envelope.

In our model of AFGL 2591 (Table 1) we use a mass infall rate determined from a comparison of Eq. 3 with the van der Tak et al. (1999) expression for number density and assuming the infalling cloud material to be molecular hydrogen. We adopt a value of 15° for the cavity half opening angle (see van der Tak et al. 1999; Poelman & van der Tak 2007). The stellar wind velocity is chosen to agree with an early B-type star. The disk wind velocity agrees well with the $\sim$ 500 km s^{-1} velocities inferred from the observed high-velocity wings of infrared absorption lines (van der Tak et al. 1999). Our model results show a count rate of 0.09 ks^{-1} which is consistent with the conservative upper-limit of 0.2 ks^{-1}. The visual exctinction to the star ($A_{\rm v} \simeq 105$ mag) agrees well with the 100 mag determined by van der Tak et al. (1999) from JCMT observations of the C^{17}O J=2→1 and J=3→2 lines. The molecular gas with velocities of $\sim$ 200 km s^{-1} observed by van der Tak et al. (1999) and interpreted as the entrainment of cloud material by the ionized wind outflow can be readily explained by our winds-cavity model.

[3] http://cxc.harvard.edu/cda/

5 DISCUSSION

For model R1 the efficiencies for converting the mechanical wind power into thermal energy and then into X-ray emission ($= L_{\rm int}/\zeta$) are $\simeq 5 \times 10^{-6}$ and $\simeq 9 \times 10^{-4}$ for the stellar and disk winds respectively, where ζ is the power of the specified wind. These values are representative of those calculated for all of the models with a common trend being that the efficiency is roughly two orders of magnitude higher for the disk wind. In many cases the disk wind dominates the attenuated X-ray emission, despite the mechanical power being typically less than that from the faster stellar wind. However, the faster stellar wind is always responsible for the hardest X-ray emission.

The model can provide a match to the observed X-ray characteristics of a sample of MYSOs. The intrinsic variability to the observed emission, caused by the dynamics and fluctuations in the position of the reverse shock, complicates placing constraints on model parameters. One possible avenue for future work would be to attempt simultaneous fits to radio observations with the models.

A recurring feature of the simulations was the delicate balance between the infall and the outflow. It proved impossible to attain a set of parameters where the cavity wall remained stable and roughly stationary for $t \simeq 10^4$ yr. The cause of this problem is the imbalance between the pressure in the infalling material and that in the outflows. Noting that the method used to describe the shape of the cavity wall is essentially arbitrary, a more realistic approach would be to have an initially fully embedded MYSO and to create a self-consistent cavity via a jet/outflow.

Intuitively one would expect the opening angle of a cavity to be tied to the evolution of the central star(s), and that an initially narrow cavity resulting from a molecular outflow would be widened by outflows as the star evolves to finally be revealed as a main sequence star (e.g. Velusamy & Langer 1998). In a recent paper, Cantó et al. (2008) modelled outflow cavities using a prescription with a time dependent opening-angle for the outflow. Although observational results could be qualitatively reproduced, it is unclear from the wind-cavity models whether such an approach is physically realistic.

The model used in this paper considers the central object to be a single star. However, most massive stars form in binaries, which allows the collision of winds between the stars as well (e.g. Stevens et al. 1992; Parkin & Pittard 2008; Pittard 2009), and could potentially generate considerably more X-ray emission (e.g. Parkin et al. 2009).

6 CONCLUSIONS

Hydrodynamical simulations of the wind-cavity interaction around an embedded MYSO have been studied. The latitude dependent wind geometry we use incorporates both a stellar and disk wind. Using an extensive range of simulations we have examined the effect of varying different model parameters on the evolution of the cavity and the resulting observational characteristics (i.e. column densities, X-ray luminosities and count rates). The main conclusions from this work are:

- The collision of the winds against the cavity wall generates a reverse shock (for cavity half opening angles $\omega \lesssim 60^\circ$) close to the star ($\lesssim 500$ au). The shock heated gas produces X-ray emission with an integrated count rate and spatial extent in agreement with observations of MYSOs by *Chandra*. The position and shape of the reverse shock is dependent on the ram pressure in the inflow/outflow. Fluctuations in the position of the reverse shock cause variability of the observed emission on timescales of several hundred years, and possibly on shorter timescales which were not probed.
- The amount of X-ray emission in the 4-10 keV band is dependent on the position of the reverse shock, which is strongly related to the stellar wind speed and the adopted mass inflow and outflow rates.
- Integrated count rates in agreement with *Chandra* detections of MYSOs are obtained across a wide region of model parameter space, indicating that the generation of X-ray emission through the interaction of an outflow with infalling material is potentially a very robust process.
- There is a limiting opening angle of the cavity for which a reverse shock is produced which resides close to the star and encloses the unshocked winds. For our adopted wind geometry we find this (full) opening angle to be 120°.
- There appears to be a delicate hydrodynamic balance between the inflow and outflow.

The model presented in this work provides a useful first insight into the interaction between winds from an MYSO and the surrounding envelope. As with many astrophysical problems, there is a vast range of scales to consider in modelling the wind-cavity interaction, and the methods employed dictate the approximations that must be made. To accurately model the driving of the winds requires high resolution in the wind acceleration region (e.g. Proga et al. 1998). Future models would benefit greatly from higher resolution in the region close to the star and disk. This would allow the interaction between the outflow and inflow from the acceleration of the disk wind to the intersection point between the disk wind and the cavity to be examined. This would be an improvement on the current work as it would allow the stellar and disk winds to be self-consistently driven and the photoevaporation of the accretion disk (e.g. Hollenbach et al. 1994; Richling & Yorke 2000) could be examined. On larger scales, the evolution of the HII region around the star could be followed.

Acknowledgements

ERP thanks the University of Leeds for funding through a Henry Ellison Scholarship. JMP gratefully acknowledges funding from the Royal Society. We thank the anonymous referee for helpful comments which improved the presentation of this paper.

REFERENCES

Alvarez, C., Hoare, M., & Lucas, P. 2004a, A&A, 419, 203
Alvarez, C., Hoare, M., Glindemann, A., & Richichi, A. 2004b, A&A, 427, 505
Banerjee, R. & Pudritz, R. E. 2006, ApJ, 641, 949
Banerjee, R. & Pudritz, R. E. 2007, ApJ, 660, 479
Beltrán, M. T., Cesaroni, R., Codella, C., Testi, L., Furuya, R. S., & Olmi, L. 2006, Nature, 443, 427

Benz, A. O., Stäuber, P., Bourke, T. L., van der Tak, F. F. S., van Dishoeck, E. F., & Jørgensen, J. K. 2007, A&A, 475, 549
Beuther, H., Schilke, P., Gueth, F., McCaughrean, M., Andersen, M., Sridharan, T. K., & Menten, K. M. 2002, A&A, 387, 931
Blondin, J. M., Kallman, T. R., Fryxell, B. A., & Taam, R. E. 1990, ApJ, 356, 591
Broos, P., Townsley, L., Getman, K., & Bauer, F. 2002, ACIS Extract, An ACIS Point Source Extraction Package. Pennsylvania State University
Broos, P. S., Feigelson, E. D., Townsley, L. K., Getman, K. V., Wang, J., Garmire, G. P., Jiang, Z., & Tsuboi, Y. 2007, ApJS, 169, 353
Bunn, J. C., Hoare, M. G., & Drew, J. E. 1995, MNRAS, 272, 346
Cantó, J., Raga, A. C., & Williams, D. A. 2008, Revista Mexicana de Astronomia y Astrofisica, 44, 293
Carpenter, J. & Hodapp, K. 2008, ArXiv e-prints
Cassen, P. & Moosman, A. 1981, Icarus, 48, 353
Chevalier, R. A. 1983, ApJ, 268, 753
Colella, P. & Woodward, P. R. 1984, Journal of Computational Physics, 54, 174
Cox, A. N. 2000, Allen's astrophysical quantities. Allen's Astrophysical Quantities
Crapsi, A., van Dishoeck, E. F., Hogerheijde, M. R., Pontoppidan, K. M., & Dullemond, C. P. 2008, A&A, 486, 245
Cunningham, A., Frank, A., & Hartmann, L. 2005, ApJ, 631, 1010
Davis, C. J., Varricatt, W. P., Todd, S. P., & Ramsay Howat, S. K. 2004, A&A, 425, 981
Delamarter, G., Frank, A., & Hartmann, L. 2000, ApJ, 530, 923
Dougherty, S. M., Pittard, J. M., Kasian, L., Coker, R. F., Williams, P. M., & Lloyd, H. M. 2003, A&A, 409, 217
Drew, J. E., Bunn, J. C., & Hoare, M. G. 1993, MNRAS, 265, 12
Drew, J. E., Proga, D., & Stone, J. M. 1998, MNRAS, 296, L6+
Felli, M., Massi, M., Staude, H. J., Reddmann, T., Eiroa, C., Hefele, H., Neckel, T., & Panagia, N. 1984, A&A, 135, 261
Freeman, P. E., Kashyap, V., Rosner, R., & Lamb, D. Q. 2002, ApJS, 138, 185
Fruscione, A., et al. 2006, in Society of Photo-Optical Instrumentation Engineers (SPIE) Conference Series Vol. 6270 of Society of Photo-Optical Instrumentation Engineers (SPIE) Conference Series, CIAO: Chandra's data analysis system
Garay, G. & Lizano, S. 1999, PASP, 111, 1049
Gardiner, T. A., Frank, A., & Hartmann, L. 2003, ApJ, 582, 269
Giardino, G., Favata, F., & Micela, G. 2004, A&A, 424, 965
Gibb, A. G. & Hoare, M. G. 2007, MNRAS, 380, 246
Hoare, M. G. 2006, ApJ, 649, 856
Hoare, M. G., Drew, J. E., Muxlow, T. B., & Davis, R. J. 1994, ApJ, 421, L51
Hollenbach, D., Johnstone, D., Lizano, S., & Shu, F. 1994, ApJ, 428, 654
Hosokawa, T. & Omukai, K. 2009, ApJ, 691, 823
Howarth, I. D. & Prinja, R. K. 1989, ApJS, 69, 527
Kohno, M., Koyama, K., & Hamaguchi, K. 2002, ApJ, 580, 626
Krumholz, M. R., Klein, R. I., McKee, C. F., Offner, S. S. R., & Cunningham, A. J. 2009, ArXiv e-prints
Krumholz, M. R., McKee, C. F., & Klein, R. I. 2005, ApJ, 618, L33
Lada, C. J., Thronson, Jr., H. A., Smith, H. A., Schwartz, P. R., & Glaccum, W. 1984, ApJ, 286, 302
Lawrence, A., et al. 2007, MNRAS, 379, 1599
Lee, C.-F., Stone, J. M., Ostriker, E. C., & Mundy, L. G. 2001, ApJ, 557, 429
Liedahl, D. A., Osterheld, A. L., & Goldstein, W. H. 1995, ApJ, 438, L115
Lucas, P. W., et al. 2008, MNRAS, 391, 136
Mendoza, S., Cantó, J., & Raga, A. C. 2004, Revista Mexicana de Astronomia y Astrofisica, 40, 147
Mitchell, G. F., Hasegawa, T. I., & Schella, J. 1992, ApJ, 386, 604
Owocki, S. P., Castor, J. I., & Rybicki, G. B. 1988, ApJ, 335, 914
Parkin, E. R. & Pittard, J. M. 2008, MNRAS, 388, 1047
Parkin, E. R., Pittard, J. M., Corcoran, M. F., Hamaguchi, K., & Stevens, I. R. 2009, MNRAS, 394, 1758
Patel, N. A., et al. 2005, Nature, 437, 109
Pease, D. O., Drake, J. J., & Kashyap, V. L. 2006, ApJ, 636, 426
Pittard, J. M. 2007, Mass-Loaded Flows. pp 245–+
Pittard, J. M. 2009, MNRAS, 396, 1743
Poelman, D. R. & van der Tak, F. F. S. 2007, A&A, 475, 949
Preibisch, T., Balega, Y. Y., Schertl, D., & Weigelt, G. 2002, A&A, 392, 945
Preibisch, T., Balega, Y. Y., Schertl, D., & Weigelt, G. 2003, A&A, 412, 735
Prinja, R. K. 1989, MNRAS, 241, 721
Proga, D. 2003, ApJ, 585, 406
Proga, D., Stone, J. M., & Drew, J. E. 1998, MNRAS, 295, 595
Proga, D., Stone, J. M., & Drew, J. E. 1999, MNRAS, 310, 476
Racine, R. 1968, AJ, 73, 233
Reipurth, B. & Bally, J. 2001, ARA&A, 39, 403
Richling, S. & Yorke, H. W. 2000, ApJ, 539, 258
Saxton, C. J., Bicknell, G. V., Sutherland, R. S., & Midgley, S. 2005, MNRAS, 359, 781
Schneider, N., Bontemps, S., Simon, R., Jakob, H., Motte, F., Miller, M., Kramer, C., & Stutzki, J. 2006, A&A, 458, 855
Schneider, N., Simon, R., Kramer, C., Stutzki, J., & Bontemps, S. 2002, A&A, 384, 225
Shang, H., Allen, A., Li, Z.-Y., Liu, C.-F., Chou, M.-Y., & Anderson, J. 2006, ApJ, 649, 845
Shepherd, D. 2005, in Cesaroni R., Felli M., Churchwell E., Walmsley M., eds, Massive Star Birth: A Crossroads of Astrophysics Vol. 227 of IAU Symposium, Massive star outflows. pp 237–246
Sim, S. A., Drew, J. E., & Long, K. S. 2005, MNRAS, 363, 615
Solf, J. & Carsenty, U. 1982, A&A, 113, 142
Staude, H. J., Lenzen, R., Dyck, H. M., & Schmidt, G. D. 1982, ApJ, 255, 95

Stevens, I. R., Blondin, J. M., & Pollock, A. M. T. 1992, ApJ, 386, 265
Strickland, R. & Blondin, J. M. 1995, ApJ, 449, 727
Terebey, S., Shu, F. H., & Cassen, P. 1984, ApJ, 286, 529
Torrelles, J. M., Patel, N. A., Curiel, S., Ho, P. T. P., Garay, G., & Rodríguez, L. F. 2007, ApJ, 666, L37
Ulrich, R. K. 1976, ApJ, 210, 377
van der Tak, F. F. S. & Menten, K. M. 2005, A&A, 437, 947
van der Tak, F. F. S., van Dishoeck, E. F., Evans, II, N. J., Bakker, E. J., & Blake, G. A. 1999, ApJ, 522, 991
van der Tak, F. F. S., Walmsley, C. M., Herpin, F., & Ceccarelli, C. 2006, A&A, 447, 1011
Velusamy, T. & Langer, W. D. 1998, Nature, 392, 685
Wang, J., Feigelson, E. D., Townsley, L. K., Román-Zúñiga, C. G., Lada, E., & Garmire, G. 2009, ApJ, 696, 47
Wang, J., Townsley, L. K., Feigelson, E. D., Getman, K. V., Broos, P. S., Garmire, G. P., & Tsujimoto, M. 2007, ApJS, 168, 100
Wilkin, F. P. & Stahler, S. W. 2003, ApJ, 590, 917
Wolfire, M. G. & Cassinelli, J. P. 1987, ApJ, 319, 850
Yamashita, T., et al. 1987, PASJ, 39, 809
Yorke, H. W. & Sonnhalter, C. 2002, ApJ, 569, 846
Zinnecker, H. & Yorke, H. W. 2007, ARA&A, 45, 481